

Stem cell regulators drive a G1 duration gradient during plant root development

Received: 24 January 2025

Accepted: 14 August 2025

Published online: 18 September 2025

 Check for updates

Clara Echevarría^{1,8}, Bénédicte Desvoves^{1,8} , Marco Marconi²,
José Manuel Franco-Zorrilla³ , Laura Lee⁴ , Masaaki Umeda⁵,
Robert Sablowski⁶ , Kenneth D. Birnbaum⁴ , Krzysztof Wabnik^{2,7}  &
Crisanto Gutierrez¹ 

Organogenesis relies on the coordination of cell proliferation with developmental programs. In meristems, where new plant organs initiate, the cell proliferation potential depends on stem cell regulators, but the mechanisms linking their local activity with the cell cycle machinery remain unknown. Here we show a positional gradient of G1 duration in the *Arabidopsis* root meristem spanning from ~2 h near the meristem boundary to more than 20 h in the early stem cell derivatives. Mutations in the stem cell regulatory *PLETHORA* (*PLT*) genes and the cell cycle *RETINOBLASTOMA-RELATED 1* gene shortened G1 duration, abolishing the G1 duration gradient, whereas *PLT2* overexpression increased G1 duration. Data-driven computer modelling supported the presence of an incoherent feed-forward loop. We found that *PLT* genes are drivers with simultaneous and opposing roles in maintaining stem cell activity and inhibiting G1 progression through a cascade involving the CDK inhibitor KRP5, a *PLT* target and *RETINOBLASTOMA-RELATED 1*. The G1 duration gradient is developmentally regulated and established after the emergence of lateral roots from the primary root and correlates with increased tolerance to genome damage. Our study establishes a previously undescribed proximal–distal G1 duration gradient during root development that is shaped by the balanced activity of stem cell maintenance and cell cycle regulators.

Organogenesis requires the production of new cells together with the establishment of different organ domains and cell types directed by patterning genes. A fundamental challenge in cellular and developmental biology is to understand the coordination between cell patterning cues and cell division mechanisms. In animals, the cell cycle phase in which inductive cues are received can dictate the choice of cell fate and the switch to pluripotency¹. In plants, cell patterning decisions are integrated with cell division^{2–4}. However, the pathways linking cell cycle progression

to spatial–temporal dynamics of upstream developmental cues are not well understood. In fact, the molecular basis of cell cycle phase progression in a developmental context is largely unknown. This lack of knowledge stems from the difficulties in measuring cell cycle phase parameters at single-cell resolution in a developing organ, in particular G1, despite being a potential control point for cell fate specification⁵.

To address this question, we focused on the root apical meristem (RAM) of *Arabidopsis thaliana* (Extended Data Fig. 1), since it is

¹Centro de Biología Molecular Severo Ochoa, CSIC-UAM, Madrid, Spain. ²Centro de Biotecnología y Genómica de Plantas, UPM-INIA-CSIC, Pozuelo de Alarcón (Madrid), Spain. ³Centro Nacional de Biotecnología, CSIC, Madrid, Spain. ⁴Department of Biology, Center for Genomics and Systems Biology, New York University, New York, NY, USA. ⁵Graduate School of Science and Technology, Nara Institute of Science and Technology, Nara, Japan. ⁶Cell and Developmental Biology Department, John Innes Centre, Norwich Research Park, Norwich, UK. ⁷Departamento de Biotecnología-Biología Vegetal, Escuela Técnica Superior de Ingeniería Agronómica, Alimentaria y de Biosistemas, Universidad Politécnica de Madrid, Madrid, Spain. ⁸These authors contributed equally: Clara Echevarría, Bénédicte Desvoves. ✉e-mail: bdesvoves@cbm.csic.es; k.wabnik@upm.es; cgutierrez@cbm.csic.es

amenable for live imaging and it possesses a stereotyped anatomy, allowing us to visually track cell lineages from the stem cell up to the differentiated state. The *PlaCCI Arabidopsis* line⁶ is an ideal tool to directly measure G1 duration since the CDT1a–CFP marker starts to accumulate soon after mitosis and is rapidly degraded at the G1/S transition.

The analysis of time-lapse images acquired over 20 h (Fig. 1a,b and Supplementary Video 1) revealed that the amount of CDT1a–CFP-labelled nuclei (G1 cells) correlated inversely with the distance from the stem cell niche. G1 duration thus followed a gradient in all tissues analysed (trichoblasts, atrichoblasts, cortex and endodermis) that changed from ~2–4 h in cells near the RAM boundary (the proximal region of the RAM) up to ≥20 h in the more distal half of the RAM, close to the stem cell niche (Fig. 1c).

It is generally assumed that cell cycle duration is constant in the transit amplifying compartment that constitutes most of the RAM^{7–9}. However, some recent reports suggest a gradient of cell cycle duration from the stem cells towards the RAM boundary^{10,11}. Our results show that the G1 duration was generally longer in most cells in the distal half of the RAM than the average cell cycle values reported, considering a constant cell cycle along the RAM (-20.8 ± 2.5 h)¹².

In one of the few attempts to measure cell cycle phase duration along the meristem, early studies with irradiated root cells found a long G1 duration in cells around the quiescent centre (QC)¹³. However, the *PlaCCI* marker line revealed that G1 duration is organized in a proximal–distal graded pattern (Fig. 1c). Thus, not only the stem cells but also their early derivatives (up to ~1/3 of the RAM) develop considerably longer G1 phases than rapidly cycling cells in the more shootward half of the RAM. Furthermore, since the proximal–distal axis of the RAM correlates with the developmental trajectory of root cells, our results reveal that G1 duration is regulated along the RAM.

To check whether the long G1 duration is due to delayed CDT1a loading, we determined the time between anaphase and the first detectable CDT1a signal along the RAM (Fig. 1d). The differences were relatively small compared with the total G1 length and thus insufficient to explain the G1 duration gradient along the longitudinal RAM axis (Fig. 1e). Also, although variability exists in CDT1a accumulation, it does not correlate with a proximal–distal gradient (Fig. 1e). We therefore concluded that the G1 phase duration of stem cells and their derivatives within the proliferation domain of the RAM is dictated by a slow G1 progression and not merely by the CDT1a accumulation kinetics.

G1 progression is primarily restricted by the RETINOBLASTOMA-RELATED 1 (RBR1) protein³. To determine whether the G1 duration gradient in the RAM is dependent on RBR1, we followed G1 progression by live imaging in RAM cells in *RBR1* loss-of-function mutant plants, using a viable line (*rRBr*) in which RBR1 is silenced by RNA interference (RNAi) specifically in RAM cells¹⁴. Unlike wild-type meristems, where CDT1a–CFP-positive cells accumulate in the distal part of the RAM (Fig. 1a), the *rRBr* meristems showed significantly fewer CDT1a–CFP-positive cells, indicating a more rapid G1 progression than the wild type in the distal meristem⁶ (Fig. 1f, left, and Supplementary Video 2). Time-lapse experiments showed that 89.5% of cells in the whole RAM progress through G1 in less than ~5 h in the absence of RBR1, and consequently the proximal–distal G1 duration gradient observed in the wild type is fully abolished (Fig. 1f, right, and Extended Data Fig. 2). We thus concluded that RBR1 directly establishes the G1 duration gradient along the proximal–distal root axis, primarily by restricting G1 progression more efficiently towards the distal half of the RAM.

We also sought to determine whether other phases of the cell cycle offset the G1 gradient to keep the entire cell cycle duration constant. One possibility is that delayed or prolonged G2 progression along the meristem counterbalances the shortening of G1 duration. We measured the average G2 duration by quantifying the appearance of labelled mitotic figures in a pulse–chase experiment, in which S-phase cells were labelled with the thymidine analog 5-ethynyl-2'-deoxyuridine (EdU) and then chased for increasing periods of time with thymidine¹⁵

(Extended Data Fig. 3a) and found small differences between the epidermal (trichoblasts) (~4.5 h) and cortex and endodermal (~3.5 h) cell layers (Extended Data Fig. 3b). We also measured the G2 duration of individual cells along the RAM by recording positional information on EdU-labelled mitosis (Extended Data Fig. 4a). We noticed that EdU-labelled mitosis tended to appear earlier in the distal half of the RAM (~40% the total distance between the QC and the RAM boundary), indicating a slightly faster G2 in the distal half of the RAM than in the proximal half (Extended Data Fig. 4b), consistent with previous results obtained for the epidermis¹⁶. We used time-lapse live imaging to measure in individual cells the accumulation/degradation kinetics of CYCB1;1, a marker of cells from mid-G2 to late metaphase. Although the extent of detectable CYCB1;1 varied, this was not related to the relative position along the RAM (Extended Data Fig. 4c,d). We therefore concluded that the small variations in G2 progression rate do not compensate for the large variation in G1 duration along the RAM.

We next aimed to identify the regulatory network underlying the G1 duration gradient. To this end, we analysed transcriptomic datasets of root cell types¹⁷ searching for genes displaying a variable expression pattern along the RAM that could show a relationship with the G1 gradient. An unbiased clustering of the 1,472-gene subset with a variable expression, using a weighted correlation network analysis¹⁸, led us to identify highly correlated gene expression patterns (Supplementary Table 1). The seven different patterns (M1 through M7) could be classified into three groups, corresponding to genes with high expression only in the RAM (type A), in the middle of the root (type B) or up in the differentiated zone of the root (type C; Extended Data Fig. 5a and Supplementary Table 1).

To identify putative transcriptional regulators that could contribute to the different expression profiles, we searched for enriched transcription factor (TF) binding sites in the promoters of genes in each module (Fig. 2a). Focusing on the M1 module, which contained genes highly expressed in the distal half of the RAM with a profile similar to the G1 duration gradient, we identified a high score enrichment for binding sites of APETALA2–AINTEGUMENTA (AP2–ANT), bHLH and SQUAMOSA PROTEIN BINDING TF family members. The AP2–ANT family caught our attention since it contains the AINTEGUMENTA-like (AIL)/PLETHORA (PLT) TFs with consensus binding sites kgCACGrwtyyCgAGrmrr and gCaCGrwTyyCgAkr, respectively (nucleotide codes: K, G/T; R, A/G; W, A/T; Y, C/T; M, A/C) for PLT1 and AIL6 (ref. 19) (Extended Data Fig. 5b). These are well-known patterning genes with a graded expression in the RAM that control stem cell activity, confer cell proliferation potential and establish the longitudinal zonation in the RAM^{20–22}. PLT proteins therefore fit with the features required to behave as a molecular driver of G1 length.

Single mutants of the four *PLT* genes do not exhibit a strong difference in root phenotype, but *plt1-4*, *plt2-2* and *plt1-4*, *plt2-2*, *plt3-1* possess highly reduced root meristems with early root growth arrest, while higher-order mutants exhibit rootless phenotypes^{20,22}. We thus expressed the *PlaCCI* markers in the *plt1-4*, *plt2-2* double mutant background (Fig. 2b and Supplementary Video 3). RAM size was highly reduced in the *plt1-4*, *plt2-2* double mutant, as reported^{20–22}. In addition, quantification of G1 duration by live imaging showed that the gradient observed in the wild type (Fig. 2e) was fully abolished in the *plt1-4*, *plt2-2* double mutant (Fig. 2f and Extended Data Fig. 6). This further supports the idea that PLT and RBR1 proteins are necessary to establish the G1 gradient in the root meristem. To determine whether PLT proteins are also sufficient to restrict G1 progression in the RAM, we used plants constitutively expressing a GR-inducible version of PLT2 (ref. 23) in a *PlaCCI* marker background (Fig. 2c,d and Supplementary Video 4). Quantification of G1 duration clearly showed that cells developed much longer G1 after PLT2 induction than the wild type, in particular in the proximal half of the RAM (Fig. 2g). In fact, cells in the RAM hardly completed a G1 phase during the course of the experiment. PLT2 is therefore necessary and sufficient to modulate the G1 duration gradient.

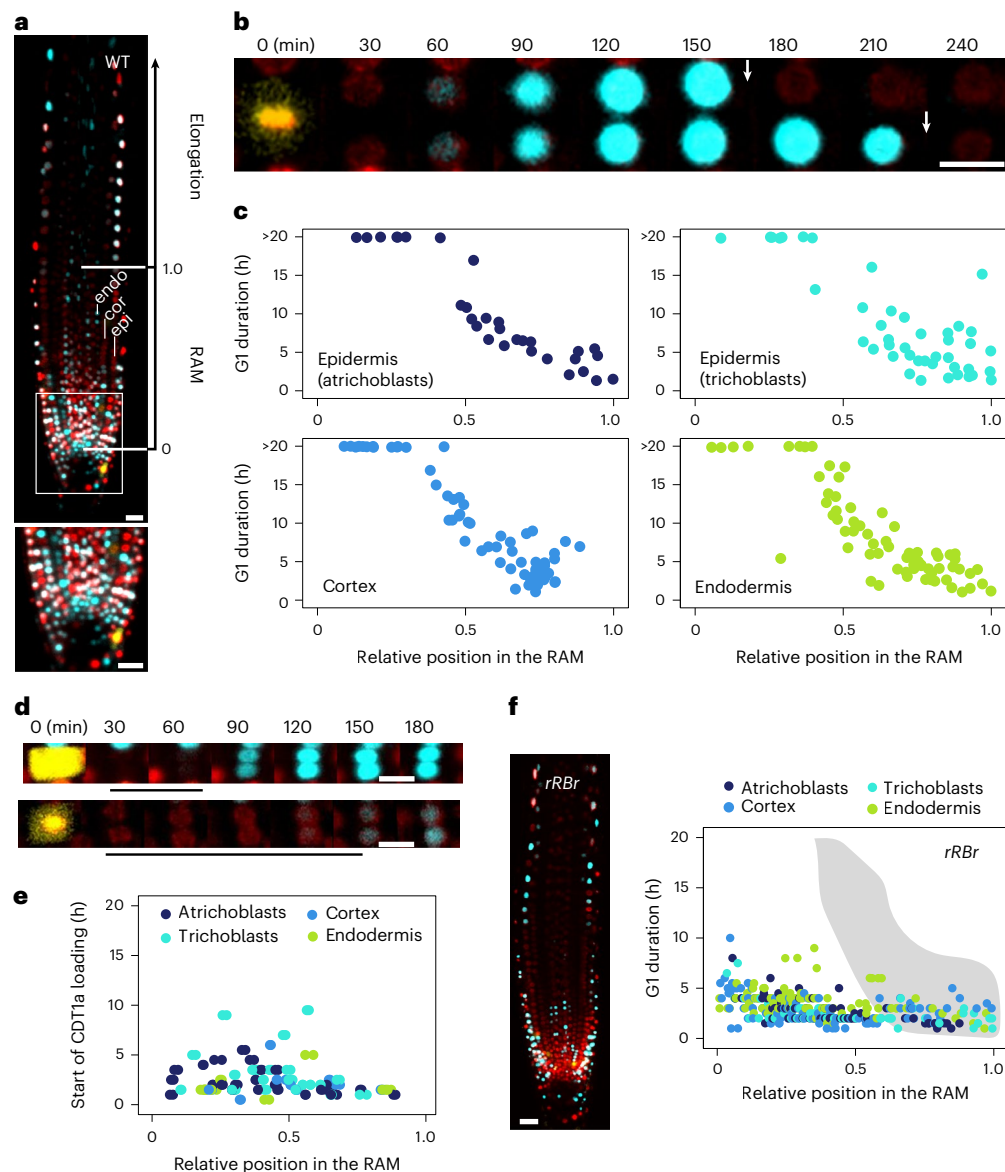


Fig. 1 | Root stem cells and early derivatives develop long G1 under control of the RBR1 pathway. **a**, Top: a root tip of the three-colour cell cycle marker line PlaCCI showing nuclei in G1 (cyan), S + early G2 (red) and late G2 + M (yellow). The image includes the RAM at the tip, followed by the elongation zone in the upper part of the root. Bottom: enlarged view of the white square in the top image, focusing on the QC, the stem cell niche and the surrounding early derivatives. The epidermal (epi) layer, which contains atrichoblasts and trichoblasts that will give rise to non-hair and hair cells, respectively, in the differentiated part of the root; cortical (cor) layer; and endodermal (endo) layer are indicated. The position of the QC is set as 0.0 and the RAM boundary as 1.0 in this and subsequent figures. This is a representative image of more than ten different roots imaged. Scale bars, 20 μ m. WT, wild type. **b**, Live-imaging example showing an epidermal cell (trichoblast), located at position 0.76 of the RAM, in metaphase (0 min). After division, the two daughter cells load CDT1a (cyan). Since CDT1a is rapidly degraded at the G1/S transition (vertical white arrows), it is a proxy of G1 duration. Scale bar, 10 μ m. **c**, G1 duration in four root cell types (atrichoblasts, trichoblasts,

cortex and endodermis), as indicated, along the RAM. The position of the QC is set as 0.0 and the RAM boundary as 1.0. The data points correspond to the G1 duration of individual cells quantified from different recorded videos (up to 20 h long using confocal microscopy). The numbers of cells recorded were 37, 46, 68 and 76 for atrichoblasts, trichoblasts, cortex and endodermis, respectively, taken from five roots. **d**, Live imaging of cells showing the period from metaphase/anaphase until the initiation of CDT1a loading. Examples of a short (top) and a long (bottom) period of CDT1a loading initiation (black lines) are shown. Scale bars, 10 μ m. **e**, Quantification of CDT1a loading time (between metaphase/anaphase and the first detectable CDT1a signal) along the RAM in four cell types, as indicated. Total $n = 128$ cells from four roots. **f**, Left: root tip of the *rbr1* loss-of-function mutant (*rRBr*) expressing the PlaCCI markers. Scale bar, 20 μ m. Right: G1 duration in four root cell types (atrichoblasts, trichoblasts, cortex and endodermis; $n = 62, 44, 94$ and 95, respectively, taken from nine roots), as indicated by the colour code, along the RAM in the *rRBr* mutant. The shaded shape covers all data points of G1 < 20 h shown in **c**.

Our mutant analysis showed that while PLT2 stimulates cell proliferation potential and meristem maintenance, it also inhibits G1 progression, presumably by impinging on the RBR1 pathway^{20,21}. We thus hypothesized that this dual relationship between PLT2 and cell cycle progression can be captured by an incoherent feed-forward loop (IFFL)²⁴. This would entail a common driver that regulates two

branches with simultaneous and opposing effects on the output, one conferring cell proliferation potential and another promoting an inhibition of cell cycle progression in G1 (Fig. 2b). To test whether this IFFL model could explain the G1 duration gradient, we constructed a data-driven computer model based on a previously introduced *Arabidopsis* root meristem framework²⁵ by integrating the IFFL mechanism

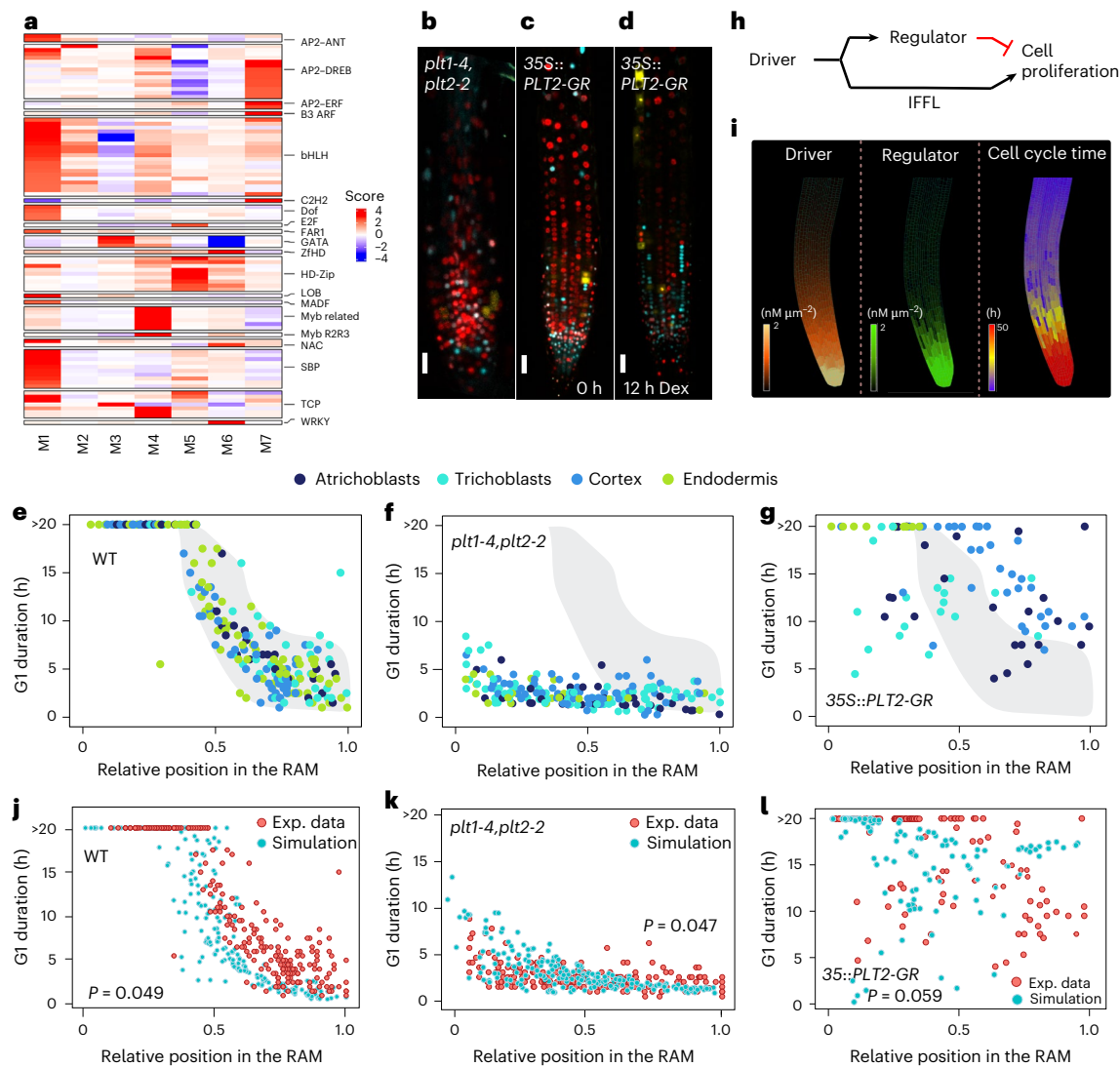


Fig. 2 | Spatial-temporal computer model of root cell proliferation for developmental control of G1. **a**, Heat map showing enrichment of TF binding sites in rows, in the gene sets from each module (M1–M7, columns as defined in Extended Data Fig. 6). TF binding sites were mapped in 1-kb regions upstream of the transcription start sites as described in Methods, and fold enrichment on a log₂ scale was calculated by mapping the same sites in the complete *Arabidopsis* promoter set. **b**, Root tip of a *plt1-4, plt2-2* double mutant in the PlaCCI marker line showing the reduced size of the RAM. Scale bar, 20 μm. **c,d**, Two representative frames of a video of the 35S::PLT2-GR line with the PlaCCI markers at 0 h (c) and 12 h (d) after treatment with Dex. Scale bar, 20 μm. **e**, Summary of G1 duration values in the wild type (taken from Fig. 1c and included here to facilitate comparison with the other genotypes). The shaded shape includes data of G1 < 20 h measured in the wild type. **f**, G1 duration in four root cell types (atrachoblasts, trichoblasts, cortex and endodermis; *n* = 36, 26, 81 and 64, respectively, from two roots), as indicated by the colour code, along the RAM in the *plt1-4, plt2-2* double mutant. The shaded shape is the same as in **e**. **g**, G1 duration in four root cell types (atrachoblasts, trichoblasts, cortex and endodermis; *n* = 24, 19, 29 and 8, respectively, from four roots), as indicated by the colour code, along the RAM in the 35S::PLT2-GR line. The shaded shape is the same as in **e** and **f**. **h**, The IFFL mechanism underlying the model. The diagram shows the main elements taking part in the model and their connections. A high

concentration of the driver in the root tip confers cell proliferation activity. In turn, the driver promotes the expression of the cell division regulator. Cell cycle phase length is inversely proportional to regulator amounts inside the cell. Thus, in the IFFL system the driver exerts a dual action stimulating cell proliferation and at the same time delaying cell cycle progression. **i**, Left: model simulation showing driver concentrations in the wild type. High concentrations of a growth regulator in the root tip induce the expression of the driver, which is allowed to diffuse along the meristem. Middle: model simulation showing regulator concentrations in the wild type. High driver concentrations in the root tip induce the expression of the regulator. Right: model simulation showing cell cycle time along the root as a result of regulator accumulation. **j–l**, Comparison between model simulation (light blue dots) and experimental data (red dots) in the wild type (**j**), the mutant with a reduction of driver expression (*plt1-4, plt2-2* for experimental data; **k**) and the mutant with a constitutive driver expression (35S::PLT2-GR line for experimental data; **l**). Each dot represents the value relative to a single cell. The *P* value indicates the probability of obtaining a similar data fit from randomized simulations based on Hausdorff distance⁵¹ and the random sampling method. *P* < 0.05 indicates significant quantitative similarity between model predictions and experimental data (see the test description in ‘Computational model description’ in Methods).

with experimental data on the spatial distribution of regulators and cell cycle characteristics (Supplementary Table 2 and Extended Data Fig. 7). Spatial-temporal model simulations predicted the pattern of cell cycle duration along the RAM axis (Fig. 2i) and quantitatively matched the experimental observations of a proximal–distal gradient of G1 duration

in the wild type (Fig. 2j). Removing the driver from the IFFL abolished the G1 gradient (Fig. 2k), while expressing it constitutively in the model increased G1 duration along the RAM (Fig. 2l), mimicking the effects of loss and gain of PLT function. The model therefore showed that a PLT-initiated IFFL circuit is a plausible fold-change detector of PLT

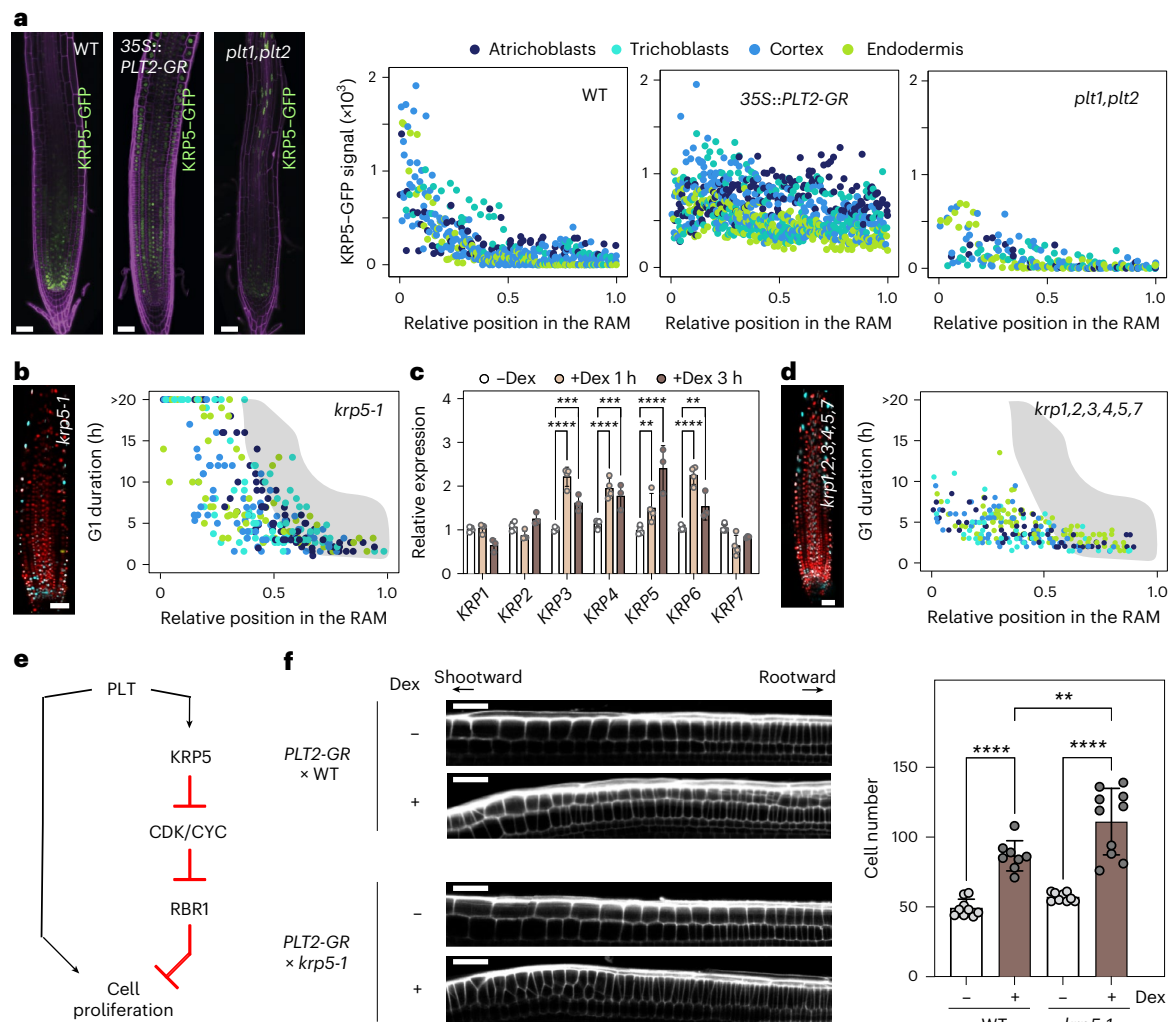


Fig. 3 | The KRP5-RBR1 pathway controls G1 duration and links with the PLT root patterning genes. a, KRP5 expression depends on PLT2. Left: root tips of plants expressing the KRP5-GFP translational fusion expressed under the *KRP5* promoter in the wild type, 35S::PLT2-GR after 22 h of Dex treatment and *plt1,plt2*. Scale bars, 20 μ m. Right: quantification of the KRP5-GFP signal along the RAM (control WT, $n = 472$ cells, four roots; 35S::PLT2-GR, $n = 818$ cells, four roots; *plt1,plt2*, $n = 183$ cells, five roots) along the RAM (0 is the QC; 1.0 is the RAM boundary). **b**, Left: root tip of a *krp5-1* mutant expressing the *PlacCI* markers. Scale bar, 20 μ m. Right: G1 duration in four root cell types (atrichoblasts, trichoblasts, cortex and endodermis; $n = 78, 73, 68$ and 59 , respectively, from six roots), as indicated, along the RAM. The shaded shape is taken from Fig. 1f and is included here to facilitate comparison with the values of G1 duration in the wild type. **c**, Transcript levels of all *KRP* genes were analysed by reverse transcription-quantitative polymerase chain reaction (RT-qPCR) in four-day-old roots of 35S::PLT2-GR plants before (-Dex, control) and after (+Dex) Dex treatment (1 h and 3 h). The expression data were normalized to *GAPC-2* (AT1G13440). The bars represent the mean \pm s.d. from three (+Dex 3 h) or four (-Dex and +Dex 1 h) biological replicates, and the individual points indicate the mean of three technical replicates for each biological replicate. Statistically significant differences were determined by a two-way analysis of variance followed by two-sided Tukey's multiple comparison tests: ** $P < 0.01$; *** $P < 0.001$; **** $P < 0.0001$. Note that the other statistically non-significant comparisons ($P > 0.05$) have

been omitted for simplicity. **d**, Left: root tip of a *krp1,2,3,4,5,7* mutant expressing the *PlacCI* markers. Scale bar, 20 μ m. Right: G1 duration in four root cell types (atrichoblasts, trichoblasts, cortex and endodermis; $n = 51, 45, 69$ and 99 , respectively, from two roots), as indicated, along the RAM. The shaded shape is taken from Fig. 1f and is included here to facilitate comparison with the values of G1 duration in the wild type. **e**, Basic components of the IFPL identified in this study that controls the developmental regulation of G1 duration in the RAM. PLT proteins that show a proximal-distal gradient in the RAM play opposing functions: they confer cell proliferation potential and also activate expression of the CDK inhibitor KRP5, which in turn restricts RBR1 phosphorylation and prolongs the G1 phase. **f**, Stimulation of cell division by PLT2 is restricted by KRP5. The 35S::PLT2-GR construct was expressed with and without Dex in the wild-type and *krp5-1* mutant backgrounds, as indicated. Left: details of the epidermal layer in the different experimental conditions. Scale bars, 20 μ m. Right: quantification of the amount of cortical cell divisions in the RAM before and after 3 h of Dex treatment. The bars represent mean \pm s.d., and the data points correspond to individual roots of the following biological replicates: 35S::PLT2-GR -Dex ($n = 9$), 35S::PLT2-GR +Dex ($n = 8$), 35S::PLT2-GR, *krp5-1* -Dex ($n = 9$) and 35S::PLT2-GR, *krp5-1* +Dex ($n = 10$). Statistical significance between genotypes was determined using one-way analysis of variance followed by Tukey's multiple comparison tests (two sided): ** $P < 0.01$; **** $P < 0.0001$.

levels²⁶ and provides a mechanism for generating the robust G1 gradient along the meristem.

To reveal the molecular link between PLT2 and G1 progression, we searched available chromatin immunoprecipitation sequencing (ChIP-seq) data and found the CDK inhibitor KRP5/ICK3 as a direct PLT2 target²³. We confirmed that the expression pattern of KRP5-GFP

shows a gradient with high levels close to the QC that progressively decreased along the RAM (Fig. 3a), less apparent in the atrichoblast cell file. This mimics the PLT gradient²¹ and closely matches the expression pattern of the negative G1 regulator predicted in the *in silico* IFPL model (Extended Data Fig. 8a). The dependence of KRP5 expression on PLT2 was further demonstrated by quantifying KRP5-GFP levels in

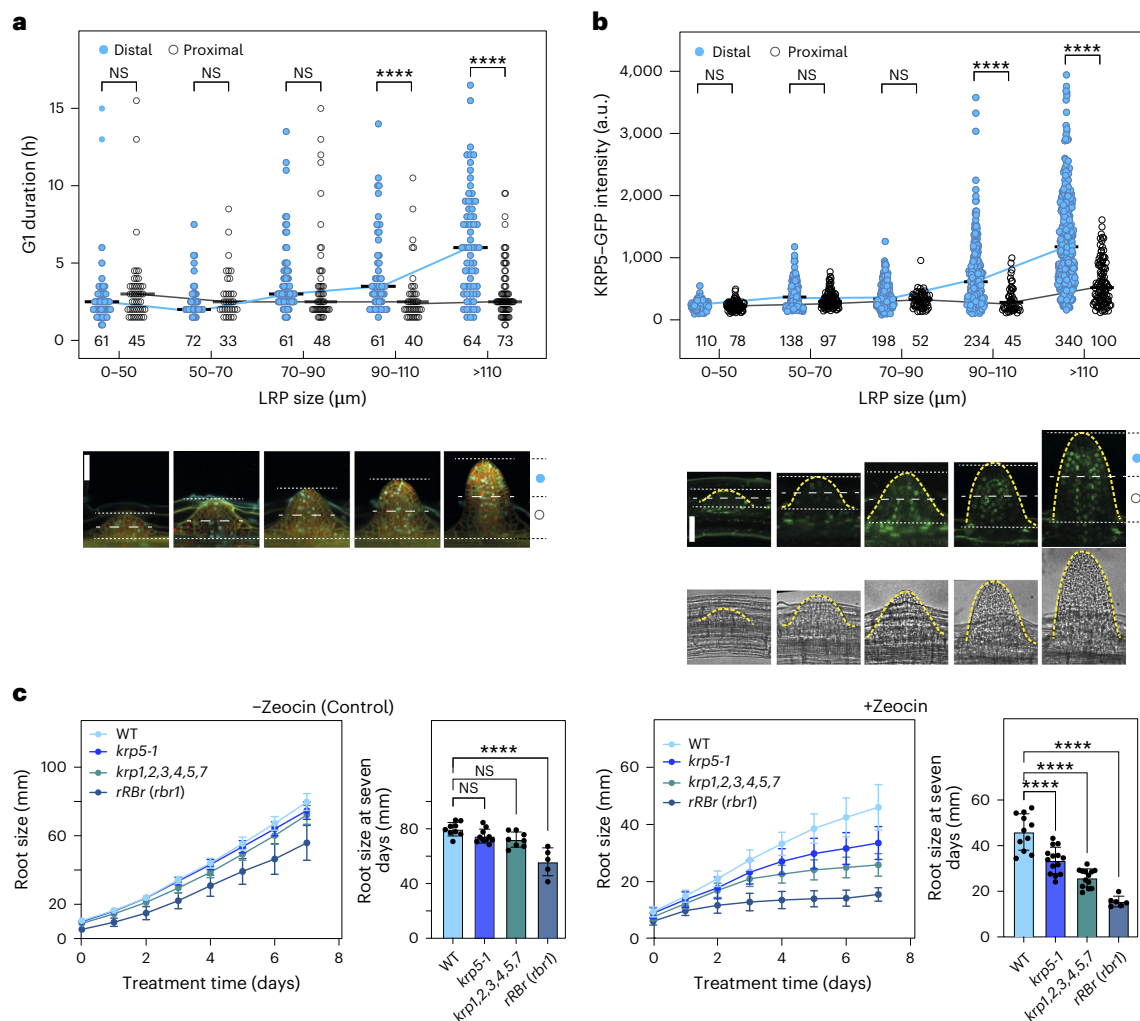


Fig. 4 | Relevance of the G1 duration gradient. **a**, G1 duration is regulated at different stages of LR development. For quantification, the LRPs of seven-day-old *Placc1* seedlings were classified by size and divided into two halves: the distal half (solid blue circles) towards the apex of the LRPs and the proximal half (empty circles) towards the base of the LRPs. The data points correspond to the G1 duration of individual cells quantified from different recorded videos (up to 21 h long using confocal microscopy), and the median is represented. The number of cells recorded is indicated for each LRP size class below each data distribution inside the graph, all collected from nine LRPs of three roots. Statistical significance was determined using non-parametric Mann–Whitney rank sum tests (two sided): NS, not significant ($P > 0.05$); **** $P < 0.0001$. Representative images of the LRPs analysed at different developmental stages are shown below the graph. Scale bar, 40 μm. **b**, KRP5 protein level is also regulated at different stages of LR development. LRPs were classified by size, as in **a**. Quantification of KRP5-GFP signal was carried out in the distal and proximal halves of the LRPs, as described in **a**. The data points correspond to the KRP5-GFP signal intensity of individual cells, and the median is represented. The number of cells recorded are indicated for each LRP size class below each data distribution inside the graph. The number of LRPs scored for each size class was $n = 6$ for 0–50, $n = 7$ for

51–70, $n = 6$ for 71–90, $n = 4$ for 91–110 and $n = 7$ for >111 from five roots. Statistical significance was determined using Mann–Whitney rank sum tests (two sided): NS, $P > 0.05$; **** $P < 0.0001$. Representative images of LRPs analysed at different developmental stages are shown below the graph. Bright-field images of the same LRPs shown are included to facilitate visualization of the LRPs (highlighted with dashed yellow lines). Scale bar, 40 μm. **c**, Plants with a G1 duration gradient show a more robust response to DNA-damaging treatments. The left plot on each side shows the root growth kinetics of plants transferred at four days post sowing to an MSS medium (as described in Methods) in the absence (control) or presence of zeocin ($2.5 \mu\text{g ml}^{-1}$) of the wild type and the indicated mutants. The right plot on each side shows the quantification of root size measured at the end of the experiment (seven days after treatment). The colour code is as indicated in the left plots. The data points correspond to individual roots. The root sample sizes were as follows: in the control treatment, $n = 9$ for the wild type, $n = 10$ for *krp5-1*, $n = 8$ for *krp1,2,3,4,5,7* and $n = 5$ for *rRB/rbr1*; in the zeocin treatment, $n = 11$ for the wild type, $n = 15$ for *krp5-1*, $n = 13$ for *krp1,2,3,4,5,7* and $n = 6$ for *rRB/rbr1*. Statistical significance was determined using one-way analysis of variance followed by two-sided Tukey’s multiple comparison tests (NS, $P > 0.05$; **** $P < 0.0001$).

the *plt1,plt2* mutant, where it was highly reduced, while high levels were maintained along the RAM in the *PLT2-GR* dexamethasone-inducible (Dex-inducible) line (Fig. 3a). The KRP5 expression gradient is therefore regulated by the *PLT2* gradient, suggesting that it can be responsible for the G1 duration gradient along the RAM.

To directly evaluate the role of KRP5 in the control of G1 duration, we expressed the *Placc1* markers in the *krp5-1* mutant background (Fig. 3b, left). We found that the *krp5-1* mutation shortened G1 in cells of the distal half of the meristem (Fig. 3b, right, Supplementary Video 5

and Extended Data Fig. 8b). We also found that ectopic *PLT2-GR* protein expression produced an increase in the KRP5 mRNA levels at short time after Dex induction but also affected mRNA levels of other KRP members (Fig. 3c). Consequently, we measured G1 duration using *Placc1* expressed in a sextuple *krp1,2,3,4,5,7* (also named *ick1,2,6,7,3,5*)²⁷ mutant background (Fig. 3d, left). We found that the G1 gradient was now abolished (Fig. 3d, right, Extended Data Fig. 8c and Supplementary Video 6), phenocopying the loss of *PLT* driver function. This also revealed that KRP6/ICK4, still present in the sextuple mutant, was not

very relevant in controlling the G1 duration gradient. A summary of the G1 duration of cells in the distal and proximal halves of the RAM in all the genotypes studied is shown in Extended Data Fig. 9.

Our data and modelling predictions jointly indicate the existence of a gene regulatory network that restricts G1 progression. Since KRPs inhibit CDK activity, which in turn relieves RBR1 repression³, the PLT2–KRP–RBR1 pathway fulfils the role of the negative regulatory branch in the IFFL model, where PLT2 acts as an upstream molecular driver (Fig. 3e). PLT2 thus drives two opposing branches acting simultaneously: one stimulating cell proliferation potential and another activating the expression of the *KRP5* CDK inhibitor, which restricts cell cycle progression by lengthening the G1 phase. Such fold-change detection of PLT levels along the root provides a robust mechanism for controlling G1 duration and hence cell proliferation patterning during root development. In this scenario, KRP5 is directly responsible for transferring the diffusion-driven PLT gradient to the RBR1 regulatory function (Fig. 3e). This is further supported genetically since the excess cell division observed in the PLT2-GR roots is highly increased in the *krrp5* mutant background, demonstrating that KRP5 restricts the stimulatory effect of PLT2 on cell division (Fig. 3f and Extended Data Fig. 10a). These findings together with the previously reported genetic interaction between PLT2 and RBR1 (ref. 20) have uncovered a new developmental mechanism controlling the longitudinal zonation of the root in terms of cell cycle progression. Our data show that the regulation of KRP5 by PLT2 provides a direct link between a regulator of stem cell maintenance and the formation of a G1 duration gradient in the root meristem. The participation of other factors reported to control meristem zonation through the regulation of *PLT* gene expression such as XAL1/AGL12 (refs. 28,29), GROWTH-REGULATING FACTORS and miR396 (refs. 30,31), and the peptide hormone root meristem growth factor RGF1 (ref. 32) in the control of G1 duration along the RAM by fine-tuning the proposed IFFL mechanism remains to be explored.

To explore the developmental relevance of the G1 duration gradient in the RAM, we focused on lateral root (LR) formation, a process where cell proliferation and differentiation are coordinated at various developmental stages³³. We observed very few cells in G1 at the early stages of LR formation, a pattern that progressively changed after LR emergence (Fig. 4a and Supplementary Videos 7 and 8). This is consistent with estimations of cell doubling times at early stages of LR development³⁴. Quantification of the G1 phase duration at different stages of LR development showed that G1 progression is fast at early stages and is lengthened as the LR develops (Fig. 4b), establishing at later stages the difference in G1 duration between the proximal and distal halves of the RAM of the newly formed LR, as observed in the primary root. Given the importance of RBR and KRP5 in regulating G1 progression and our previous findings that they participate in the inhibitory branch of the IFFL, we determined the dynamics of these two proteins at different stages of LR development. We found that RBR–YFP protein was enriched in the distal half of the LR meristem, but the levels appeared to be quite constant in both early and late LR developmental stages (Extended Data Fig. 10b), results that are consistent with its activity being primarily regulated post-translationally. In contrast, KRP5–GFP protein levels were strongly dependent on the LR developmental stage. We found that KRP5–GFP levels were very low at early LR primordia (LRP) stages, coinciding with a fast G1. At later LRP developmental stages, KRP5–GFP levels increased significantly in the distal half of LRPs, but not in the proximal half, establishing a distal–proximal gradient similar to that observed in the RAM and coinciding with the increase in G1 duration in the distal domain (Fig. 4b). Moreover, the fast production of new cells at early stages of LR development is analogous to the fast G1 progression reported in regenerating cells after root ablation before a new fully formed primary root is established³⁵. Together, these data reinforce the idea that a dynamic G1 duration is intrinsic to various conditions of organ development.

We also evaluated the possible impact of the G1 duration gradient in relation to the maintenance of genome integrity, which is of primary importance for stem cells and their early derivatives³⁶. We measured root growth after a prolonged genotoxic challenge at drug concentrations that do not arrest root growth. We found that the sextuple *krrp1,2,3,4,5,7* mutant grown in zeocin, a drug that produces double-strand breaks, showed a reduced tolerance and severely impaired root growth (Fig. 4c). The *rbr1* mutant showed an enhanced reduction of root growth, consistent with the known participation of RBR1 in G1 progression and DNA repair^{37,38}.

Our findings highlight the unexpected role of G1 duration in spatial–temporal plant organ growth where specified stem cells and early derivatives develop long G1 phases, whereas cells undergoing their last division cycles before differentiation accelerate G1 progression. Interestingly, the *Lgr5*⁺-expressing cells in intestinal crypts, a marker of stemness, also develop longer cell cycles than their late derivatives as a result of a longer G1 phase³⁹. Regulating the G1 duration gradient also raises broader questions, since it may be relevant for other growing organs in both plants and animals given the high conservation of retinoblastoma proteins in G1 progression control in all eukaryotes³. We propose that the mechanism elucidated here, possibly in coordination with others, to establish a long G1 duration in a large fraction of RAM cells favours the root lifespan. Additionally, a long G1 serves to maintain the genome integrity of stem cell derivatives, providing a growth advantage to the root in response to genotoxic challenges.

Methods

Plant material and growth conditions

The following *Arabidopsis thaliana* lines were used in this work: wild-type Columbia ecotype (Col-0) from NASC, *PlacCI⁺ pRCH1::RBR* RNAi (rRBR)⁴, *plt1-4, plt2-2* (ref. 22), *35S::PLT2-GR*²³, *krrp5-1* (TAIR accession SALK_053533)⁴⁰, sextuple *krrp1,2,3,4,5,7* (ref. 27) and *pRBR::RBR–YFP*⁴¹. Plants expressing KRP5–GFP were generated by using a construct containing a 4363 insert of a genomic fragment spanning from 2,989 bp upstream of the transcription start site to 621 bp downstream of the stop codon. The PCR-amplified genomic fragment was cloned into the Gateway entry vector pDONR221 by BP reaction according to the manufacturer's instructions (no. 11789020, Thermo Fisher Scientific), and the sGFP tag was inserted just before the stop codon by the SLICE method⁴². An attL x attR recombination with LR clonase (11791020, Thermo Fisher Scientific) was performed with the destination vector pGWB1 (ref. 43) to generate a binary vector. Seeds were bleach-sterilized, stratified at 4 °C for two days and grown on MSS medium containing 0.5× Murashige and Skoog (M0222) salts (pH 5.7) supplemented with MES (M1503), vitamins (M0409), 1% sucrose (S0809) and 0.6%, 0.8% or 1% agar (P1001), all from Duchefa. Plant transformation was carried out via the floral dip method⁴⁴. Plants grew vertically or horizontally in an incubator at 21 °C and 60% moisture, under long-day conditions (16 h light/8 h dark cycles, fluorescent tubes (Radium Spectralux Plus NL-T8), 36 W, cool daylight, 100 μmol m^{−2} s^{−1}). For chemical treatments, three-day-old plants were transferred to MSS medium with or without 2.5 μg ml^{−1} zeocin (R25001, Thermo Fisher Scientific) or to MSS medium containing either 10 μM Dex (D4902, Sigma-Aldrich) or the equivalent volume of ethanol for the control.

In vivo imaging and confocal microscopy

Seedlings were transferred four days post-sowing to P35 coverslip-bottom dishes (MatTek) and seven days post-sowing to a large coverslip chamber (Ibidi) for live imaging of the RAM and LRPs, respectively. A block of 1% agar with 0.5× Murashige and Skoog medium was placed on top of the seedlings, and a segment was cut with a sterilized blade, making room for the aerial part to grow outside of the agar. To avoid curling and drifting of the roots in the z plane, a square piece of 100-μm nylon mesh (Nitex) was placed between the seedlings and the agar

block, creating tracks for the roots to grow straight. After the lid was fixed with Micropore tape, the roots were allowed to acclimate overnight, with the dishes placed vertically in the plant culture chamber. For 35S::PLT2-GR lines, the block of agar contained 10 μ M Dex to induce PLT2-GR activity, and confocal imaging was initiated 6 h after Dex induction. Root meristems were imaged every 30 min up to 20 h with a Nikon A1R+ inverted confocal microscope using an oil \times 40 objective. Confocal stacks spanning over half the root thickness (pinhole of 3.5–4 μ m, \sim 50 μ m distributed in \sim 14 z planes) were acquired at each time point, with 2 \times 1 tile-scan to cover the whole meristem plus the transition zone length. Images and video editing were performed using Fiji v1.53f51 (ref. 45). Different root cell types were identified by their anatomical position in the root. In each case, scoring was initiated at the RAM boundary and then continuing along the file up to the QC. All imaging experiments were performed in at least two independent replicates conducted on different days.

Positioning of cells and mitotic figures in the root meristem

The positions of individual cells in the meristem were calculated by:

$$\text{Relative position} = \frac{\text{Cell distance from QC } (\mu\text{m})}{\text{Meristem length } (\mu\text{m})}$$

Meristem length was taken as the distance from the QC to the first cell doubling its size. A relative position of 0 thus corresponds to the QC and 1 to the end of the meristem. Epidermal, cortical and endodermal cell positions were relative to their own tissue meristems. When this position was calculated in the analysis of *in vivo* experiments, the cell distance from the QC was that at the beginning of the process under study—for example, right after the anaphase of a cell in which G1 was being measured. For G1 length measurement at different stages of LRP development, LRP length and cell position were determined in the time frame of cell division.

EdU labelling and chase experiments

Seedlings (seven days after sowing) were transferred to 0.5 \times liquid MSS containing 20 μ M EdU (A10044, Thermo Fisher Scientific) for 15 min to label cells undergoing S phase. The analogue was then washed off, and the plants were incubated in 0.5 \times liquid MSS supplemented with 50 μ M thymidine (Sigma) for different chase time periods to allow cell cycle progression. The plants were then fixed with 4% paraformaldehyde in microtubule stabilizing buffer (50 mM PIPES, pH 6.9, 5 mM EGTA, 5 mM MgSO₄) and permeabilized as described previously⁴⁶. EdU incorporation was detected with the Click-It Alexa Fluor 647 Imaging kit (C10640, Thermo Fisher Scientific), nuclei were stained with DAPI and roots were imaged by confocal microscopy with a Zeiss LSM800. G2 phase length was directly measured along the root meristem by determining the kinetics of appearance of EdU-labelled mitotic (Extended Data Fig. 3) in the different tissues and chase times⁸.

Analysis of the dynamics of cell cycle marker proteins

The residence time of CYCB1;1-YFP in the cells was measured by *in vivo* imaging of PlacCI seedlings⁶ as the time between the loading of this protein in G2 and its degradation at the metaphase–anaphase transition. CDT1a loading kinetics was assessed by measuring the time between the end of anaphase and a detectable CDT1a–CFP signal. Likewise, G1 phase duration was given by the time between the end of mitosis and the degradation of CDT1a–CFP at the G1/S transition.

Quantitative real-time PCR with reverse transcription

Total RNA was extracted from roots from Col-0 and PLT2-GR-expressing plants after Dex induction. Tissues were frozen in liquid nitrogen and ground with glass beads using a Silamat S5 (Ivoclar Vivadent). The homogenized tissues were then processed using the Maxwell RSC Plant RNA Kit (Promega) following the manufacturer's instructions. Total

RNA (1 μ g) was reverse transcribed using iScript Reverse Transcription Supermix (no. 1708841, BioRad), following the manufacturer's instructions. Quantitative real-time PCR was performed using iTaq Universal SYBR Green Supermix (no. 1725124, BioRad) in a 384-well CFX Opus3 Real-Time PCR System (BioRad). Quantification was based on the crossing-point calculation, using the second-derivative maximum method of absolute quantification using *GAPC-2* (AT1G13440) as the internal control. At least three biological and three technical replicates were performed for each sample. The specific primers (IDT) used for the amplification of gene sequences are listed in Supplementary Table 3.

Differential expression of TFs along the RAM

Data were taken from the spatial gene expression patterns along the root obtained from correlative root slices from the tip (slice 1) to the basal part of the root¹⁷. We first selected a set of 1,472 genes with variable expression along the root and clustered them using weighted correlation network analysis to identify modules of highly correlated genes. We obtained seven modules (M1 through M7) containing genes of highly correlated expression levels. These were classified into three groups depending on their profiles as type A, B and C modules, corresponding to the highest expression in distal (1–6), middle (6–7) or proximal slices (10–12), respectively. To identify TFs putatively contributing to the establishment of the expression profiles, we searched for enriched TF binding sites in the promoters of genes in each module. TF binding sites were mapped in 1-kb gene promoters with FIMO⁴⁷, and fold-enrichment on a log₂ scale was calculated by mapping the same sites in the complete *Arabidopsis* promoter set. A heat map was calculated for individual TF families identified. AP2–ANT binding sites enriched in M1 promoters corresponded to PLT1 (Cis-BP ID M06622_2.00) and AIL6 (Cis-BP ID M06659_2.00) with consensus sequences kgCACGrwtyyCgAGrmrr and gCaCGrwTyyCgAkr, respectively¹⁹.

Computational model description

The model was built using MorphoDynamX, a modelling platform based on MorphoGraphX⁴⁸. MorphoDynamX is an advanced modelling framework based on a geometric data structure (<http://algorithmicbotany.org/papers/laneb.th2015.html>)⁴⁹. The mechanical growth of the simulated root is based on position-based dynamics, a modern constraint-based method used to simulate physical phenomena such as cloth, deformation, fluids, fractures and rigidity⁵⁰. Chemical processes are numerically solved using the simple Euler method. The model is a customized version of the mechano-biochemical root model, and we refer the reader to the original publication for specific details of core model implementation²⁵. The model incorporates the chemical control of cell division, according to the IFFL model concept. In the model the cell division is regulated by two biochemical species, a driver and a regulator. The presence of the division driver increases the probability of cell division, while the regulator (promoted by the driver) negatively regulates the cell division cycle. High concentrations of the regulator therefore correlate with longer division cycles. The system follows the scheme described by an IFFL (Fig. 3g). The full list of parameter descriptions can be found in Supplementary Table 2. Specifically, the division driver is induced by an upstream growth promoter, which is assumed to be present at high concentrations in the root tip. The driver is allowed to diffuse between cells²¹, according to the formula:

$$\frac{dPR}{dt} = PR_{\max} \times \frac{GR^2}{GR^2 + PR_k^2} + PR_{\text{perm}} \sum_i \frac{(PR_i - PR)L_i}{\text{area}_i + \text{area}} - d_{\text{PR}} PR \quad (1)$$

PR_{\max} is the maximum level of growth-promoter-induced driver expression, PR_k is the half-max coefficient of growth-promoter-induced driver function, PR_{perm} is the driver cell permeability coefficient, d_{PR} is the driver degradation rate, GR is the growth promoter concentration

inside the current cell, PR is the driver concentration inside the current cell, $area$ is the total area of the current cell, the summation symbol indicates iteration over the m neighbour cells of the current cell, and PR_i and $area_i$ indicate the driver concentration and area of a specific neighbouring cell, respectively. L_i is the length of the membrane between the current cell and the specific neighbouring cell.

Conversely, regulator expression is promoted by the driver:

$$\frac{dIN}{dt} = IN_{\max} \times \frac{PR^2}{PR^2 + IN_k^2} - d_{IN}IN \quad (2)$$

IN_{\max} is the maximum level of driver-induced regulator function, IN_k is the half-max coefficient of driver-induced regulator function, d_{IN} is the regulator degradation rate and PR is the driver concentration inside the current cell.

The cell cycle time (the minimum amount of time between cell divisions, which here is considered directly proportional to the G1 length) is directly regulated by the regulator according to the following formula:

$$CC_{\text{cell}} = DIV_{\max} \times \left(\frac{2}{1 + e^{-DIV_{\max} \times IN}} - 1 \right) \quad (3)$$

DIV_{\max} is the maximum cell cycle time, DIV_{IN} is the exponential rate of cell cycle regulation by the regulator and IN is the concentration of the regulator inside the current cell.

Considering the aforementioned components, cell division is implemented in the simulations according to the following rules:

- Only cells inside the meristem can divide.
- Cells are allowed to divide only once they have doubled their size in length.
- The division driver allows cell division once its concentration is above a certain threshold, DIV_{prom} .
- A cell can divide only if its lifetime (the time passed since the last division) has reached the cell cycle time determined by the division regulator, CC_{cell} .
- The division regulator is degraded after cell division.
- After cell division, biochemical species are set to half of original concentrations to account for potential dilution effects.

We performed a statistical analysis to obtain hypothesis testing results for the experimental data. We calculated the Hausdorff distance⁵¹ between experimental data and model simulations for both the wild type and the mutants. Next, we generated 10,000 random pairs of data from the following formula:

$$y_i = a_i e^{-r_i x} \quad (4)$$

where $i \in [1,2]$ indicates the pair element index, $a \in (0, 50]$ indicates the curve intercept (in accordance with the maximum cell cycle length) and $r \in (0, 10]$ indicates the exponential disgrace in cell cycle length (in accordance with the observed experimental data). We calculated the Hausdorff distance for each of the previous random pairs, and finally we calculated the P value as the proportion of random distances smaller than the Hausdorff distance obtained between the experimental data and the model simulations. A small P value indicated that the observed similarity between the experimental data and model simulations is hard to explain by chance alone.

Reporting summary

Further information on research design is available in the Nature Portfolio Reporting Summary linked to this article.

Data availability

All other data are available in the main text or the [Supplementary information](#). Source data are provided with this paper.

References

1. Boward, B., Wu, T. & Dalton, S. Concise review: control of cell fate through cell cycle and pluripotency networks. *Stem Cells* **34**, 1427–1436 (2016).
2. Meyer, H. M. et al. Fluctuations of the transcription factor ATML1 generate the pattern of giant cells in the *Arabidopsis* sepal. *eLife* **6**, e19131 (2017).
3. Desvoves, B. & Gutierrez, C. Roles of plant retinoblastoma protein: cell cycle and beyond. *EMBO J.* **39**, e105802 (2020).
4. Sablowski, R. & Gutierrez, C. Cycling in a crowd: coordination of plant cell division, growth, and cell fate. *Plant Cell* **34**, 193–208 (2022).
5. Winter, C. M. et al. SHR and SCR coordinate root patterning and growth early in the cell cycle. *Nature* **626**, 611–616 (2024).
6. Desvoves, B., Arana-Echarri, A., Barea, M. D. & Gutierrez, C. A comprehensive fluorescent sensor for spatiotemporal cell cycle analysis in *Arabidopsis*. *Nat. Plants* **6**, 1330–1334 (2020).
7. Ivanov, V. B. & Dubrovsky, J. G. Estimation of the cell-cycle duration in the root meristem: a model of linkage between cell-cycle duration, rate of cell production, and rate of root growth. *Int. J. Plant. Sci.* **158**, 757–763 (1997).
8. Fiorani, F. & Beemster, G. T. S. Quantitative analyses of cell division in plants. *Plant Mol. Biol.* **60**, 963–979 (2006).
9. Pacheco-Escobedo, M. A. et al. Longitudinal zonation pattern in *Arabidopsis* root tip defined by multiple structural change algorithm. *Ann. Bot.* **118**, 763–776 (2016).
10. Rahni, R., Efroni, I. & Birnbaum, K. D. A case for distributed control of local stem cell behavior in plants. *Dev. Cell* **38**, 635–642 (2016).
11. Rahni, R. & Birnbaum, K. D. Week-long imaging of cell divisions in the *Arabidopsis* root meristem. *Plant Methods* **15**, 30 (2019).
12. Napsucialy-Mendivil, S., Alvarez-Venegas, R., Shishkova, S. & Dubrovsky, J. G. *Arabidopsis* homolog of trithorax1 (ATX1) is required for cell production, patterning, and morphogenesis in root development. *J. Exp. Bot.* **65**, 6373–6384 (2014).
13. Clowes, F. A. L. The duration of the G1 phase of the mitotic cycle and its relation to radiosensitivity. *N. Phytol.* **64**, 355–359 (1965).
14. Wildwater, M. et al. The RETINOBLASTOMA-RELATED gene regulates stem cell maintenance in *Arabidopsis* roots. *Cell* **123**, 1337–1349 (2005).
15. Echevarria, C., Gutierrez, C. & Desvoves, B. Tools for assessing cell cycle progression in plants. *Plant Cell Physiol.* **62**, 1231–1238 (2021).
16. Otero, S., Desvoves, B., Peiro, R. & Gutierrez, C. Histone H3 dynamics uncovers domains with distinct proliferation potential in the *Arabidopsis* root. *Plant Cell* **28**, 1361–1371 (2016).
17. Brady, S. M. et al. A high-resolution root spatiotemporal map reveals dominant expression patterns. *Science* **318**, 801–806 (2007).
18. Langfelder, P. & Horvath, S. WGCNA: an R package for weighted correlation network analysis. *BMC Bioinform.* **9**, 559 (2008).
19. Weirauch, M. T. et al. Determination and inference of eukaryotic transcription factor sequence specificity. *Cell* **158**, 1431–1443 (2014).
20. Galinha, C. et al. PLETHORA proteins as dose-dependent master regulators of *Arabidopsis* root development. *Nature* **449**, 1053–1057 (2007).
21. Mähönen, A. P. et al. PLETHORA gradient formation mechanism separates auxin responses. *Nature* **515**, 125–129 (2014).
22. Aida, M. et al. The PLETHORA genes mediate patterning of the *Arabidopsis* root stem cell niche. *Cell* **119**, 109–120 (2004).
23. Santuari, L. et al. The PLETHORA gene regulatory network guides growth and cell differentiation in *Arabidopsis* roots. *Plant Cell* **28**, 2937–2951 (2016).

24. Shen-Orr, S. S., Milo, R., Mangan, S. & Alon, U. Network motifs in the transcriptional regulation network of *Escherichia coli*. *Nat. Genet.* **31**, 64–68 (2002).
25. Marconi, M., Gallemí, M., Benkova, E. & Wabnick, K. A coupled mechano-biochemical model for cell polarity guided anisotropic root growth. *eLife* **10**, e72132 (2021).
26. Goentoro, L., Shoval, O., Kirschner, M. W. & Alon, U. The incoherent feedforward loop can provide fold-change detection in gene regulation. *Mol. Cell* **36**, 894–899 (2009).
27. Cao, L. et al. *Arabidopsis* ICK/KRP cyclin-dependent kinase inhibitors function to ensure the formation of one megaspore mother cell and one functional megaspore per ovule. *PLoS Genet.* **14**, e1007230 (2018).
28. Tapia-Lopez, R. et al. An AGAMOUS-related MADS-box gene, XAL1 (AGL12), regulates root meristem cell proliferation and flowering transition in *Arabidopsis*. *Plant Physiol.* **146**, 1182–1192 (2008).
29. García-Cruz, K. V. et al. The MADS-box XAANTAL1 increases proliferation at the *Arabidopsis* root stem-cell niche and participates in transition to differentiation by regulating cell-cycle components. *Ann. Bot.* **118**, 787–796 (2016).
30. Ercoli, M. F. et al. GIF transcriptional coregulators control root meristem homeostasis. *Plant Cell* **30**, 347–359 (2018).
31. Liebsch, D. & Palatnik, J. F. MicroRNA miR396, GRF transcription factors and GIF co-regulators: a conserved plant growth regulatory module with potential for breeding and biotechnology. *Curr. Opin. Plant Biol.* **53**, 31–42 (2020).
32. Matsuzaki, Y., Ogawa-Ohnishi, M., Mori, A. & Matsubayashi, Y. Secreted peptide signals required for maintenance of root stem cell niche in *Arabidopsis*. *Science* **329**, 1065–1067 (2010).
33. Winter, Z., Bellande, K. & Vermeer, J. E. M. Divided by fate: the interplay between division orientation and cell shape underlying lateral root initiation in *Arabidopsis*. *Curr. Opin. Plant Biol.* **74**, 102370 (2023).
34. Dubrovsky, J. G., Rost, T. L., Colon-Carmona, A. & Doerner, P. Early primordium morphogenesis during lateral root initiation in *Arabidopsis thaliana*. *Planta* **214**, 30–36 (2001).
35. Lee, L. R. et al. Glutathione accelerates the cell cycle and cellular reprogramming in plant regeneration. *Dev. Cell* **60**, 1153–1167.e6 (2025).
36. Rusnak, B., Clark, F. K., Vadde, B. V. L. & Roeder, A. H. K. What is a plant cell type in the age of single-cell biology? It's complicated. *Annu. Rev. Cell Dev. Biol.* **40**, 301–328 (2024).
37. Horvath, B. M. et al. *Arabidopsis* RETINOBLASTOMA RELATED directly regulates DNA damage responses through functions beyond cell cycle control. *EMBO J.* **36**, 1261–1278 (2017).
38. Biedermann, S. et al. The retinoblastoma homolog RB1 mediates localization of the repair protein RAD51 to DNA lesions in *Arabidopsis*. *EMBO J.* **36**, 1279–1297 (2017).
39. Carroll, T. D., Newton, I. P., Chen, Y., Blow, J. J. & Näthke, I. Lgr5(+) intestinal stem cells reside in an unlicensed G(1) phase. *J. Cell Biol.* **217**, 1667–1685 (2018).
40. Wen, B., Nieuwland, J. & Murray, J. A. H. The *Arabidopsis* CDK inhibitor ICK3/KRP5 is rate limiting for primary root growth and promotes growth through cell elongation and endoreduplication. *J. Exp. Bot.* **64**, 1135–1144 (2013).
41. Cruz-Ramirez, A. et al. A bistable circuit involving SCARECROW-RETINOBLASTOMA integrates cues to inform asymmetric stem cell division. *Cell* **150**, 1002–1015 (2012).
42. Motohashi, K. A simple and efficient seamless DNA cloning method using SLiCE from *Escherichia coli* laboratory strains and its application to SLiP site-directed mutagenesis. *BMC Biotechnol.* **15**, 47 (2015).
43. Nakagawa, T. et al. Development of series of gateway binary vectors, pGWBs, for realizing efficient construction of fusion genes for plant transformation. *J. Biosci. Bioeng.* **104**, 34–41 (2007).
44. Clough, S. J. & Bent, A. F. Floral dip: a simplified method for *Agrobacterium*-mediated transformation of *Arabidopsis thaliana*. *Plant J.* **16**, 735–743 (1998).
45. Rueden, C. T. et al. ImageJ2: ImageJ for the next generation of scientific image data. *BMC Bioinform.* **18**, 529 (2017).
46. Lauber, M. H. et al. The *Arabidopsis* KNOLLE protein is a cytokinesis-specific syntaxin. *J. Cell Biol.* **139**, 1485–1493 (1997).
47. Grant, C. E., Bailey, T. L. & Noble, W. S. FIMO: scanning for occurrences of a given motif. *Bioinformatics* **27**, 1017–1018 (2011).
48. Barbier de Reuille, P. et al. MorphoGraphX: a platform for quantifying morphogenesis in 4D. *eLife* **4**, 05864 (2015).
49. Lane, B. J. *Cell Complexes: The Structure of Space and the Mathematics of Modularity*. PhD thesis, Univ. Calgary (2015).
50. Tsai, T.-C. in *Encyclopedia of Computer Graphics and Games* (ed. Lee, N.) 1–5 (Springer International, 2017); https://doi.org/10.1007/978-3-319-08234-9_92-1
51. Birsan, T. & Tiba, D. One hundred years since the introduction of the set distance by Dimitrie Pompeiu. In *System Modeling and Optimization, Proc. 22nd IFIP TC7 Conference* (eds Ceragioli, F., Dontchev, A., Futura, H., Marti, K. & Pandolfi, L.) Vol 199, 35–39 (Springer, 2006).
52. Desvoyes, B., Echevarria, C. & Gutierrez, C. A perspective of cell proliferation kinetics in the root apical meristem. *J. Exp. Bot.* **72**, 6708–6715 (2021).
53. Scheres, B. Stem-cell niches: nursery rhymes across kingdoms. *Nat. Rev.* **8**, 345–354 (2007).
54. Shimotohno, A. & Scheres, B. Topology of regulatory networks that guide plant meristem activity: similarities and differences. *Curr. Opin. Plant Biol.* **51**, 74–80 (2019).
55. Salvi, E. et al. A self-organized PLT/auxin/ARR-B network controls the dynamics of root zonation development in *Arabidopsis thaliana*. *Dev. Cell* **53**, 431–443.e23 (2020).
56. Svolacchia, N., Salvi, E. & Sabatini, S. *Arabidopsis* primary root growth: let it grow, can't hold it back anymore! *Curr. Opin. Plant Biol.* **57**, 133–141 (2020).

Acknowledgements

We thank B. Scheres and R. Heidstra for providing the *rRBR* RNAi, pRBR::RBR-YFP and PLT2-GR lines and the *plt1-4*, *plt2-2* seeds; J. Murray for the *knp5-1* mutant; and H. Wang for the sextuple *knp1,2,3,4,5,7/ick1,2,6,7,3,5* mutant. We also thank the Advanced Light Microscopy Service of CBM for their assistance with image acquisition and analysis, D. Miguez for initial discussions on root modelling, M. H. Sanchez-Rebato for help with R scripts and E. Martinez-Salas, M. Serrano and members of our laboratories for comments and suggestions. This work was funded by the Spanish Ministry of Science and Innovation and Fondo Europeo de Desarrollo Regional (FEDER), grant nos. RTI2018-094793-B-I00 and PID2021-123319NB-I00 (C.G.); the European Union, grant no. 2018-AdG_833617 (C.G.); MICIU/AEI/10.13039/501100011033/FEDER, UE, grant no. PID2024-159682NB-I00 (B.D., C.G.); the Spanish Ministry of Science and Innovation, grant nos. PGC2018-093387-A407 I00 and PID2021-122158NB-I00 (K.W.); the Programa de Atracción de Talento 2017 (Comunidad de Madrid 2021-5A/BIO-20952) (K.W.); the Spanish Ministry of Science and Innovation Severo Ochoa Programme for Centres of Excellence, institutional grant nos. SEV-2016-0672 and CEX2020-000999-S (2022 to 2025) (K.W.); the Spanish Ministry of Science and Innovation, grant nos. BIO2017-86851-P and BIO2020-119451GB-I00 (J.M.F.-Z.); the National Science Foundation, grant no. IOS-1934388 (K.D.B.); the National Institutes of Health, grant no. R35GM136362 (K.D.B.); UK Biotechnology and Biological Sciences Research Council Institute Strategic Program, grant no. BB/J004588/1 (R.S.); and MEXT KAKENHI, grant nos. 17H06470, 17H06477 and 21H04715 (M.U.). The institutional support of Fundación Ramón Areces and Banco de Santander to the Centro de Biología Molecular Severo Ochoa is also acknowledged.

Author contributions

C.G., B.D. and K.W. conceptualized the project. C.E., B.D., M.M., L.L., J.M.F.-Z., R.S., M.U. and K.D.B. devised the methodology. C.E., B.D., M.M., L.L. and J.M.F.-Z. conducted the investigation. C.G., K.W., J.M.F.-Z., R.S. and K.D.B. acquired the funding. C.G. and B.D. were responsible for project administration. C.G., B.D., K.W., R.S. and K.D.B. supervised the project. C.G. and B.D. wrote the original draft of the paper. All authors reviewed and edited the paper.

Competing interests

The authors declare no competing interests.

Additional information

Extended data is available for this paper at <https://doi.org/10.1038/s41477-025-02109-3>.

Supplementary information The online version contains supplementary material available at <https://doi.org/10.1038/s41477-025-02109-3>.

Correspondence and requests for materials should be addressed to Bénédicte Desvoves, Krzysztof Wabnick or Crisanto Gutierrez.

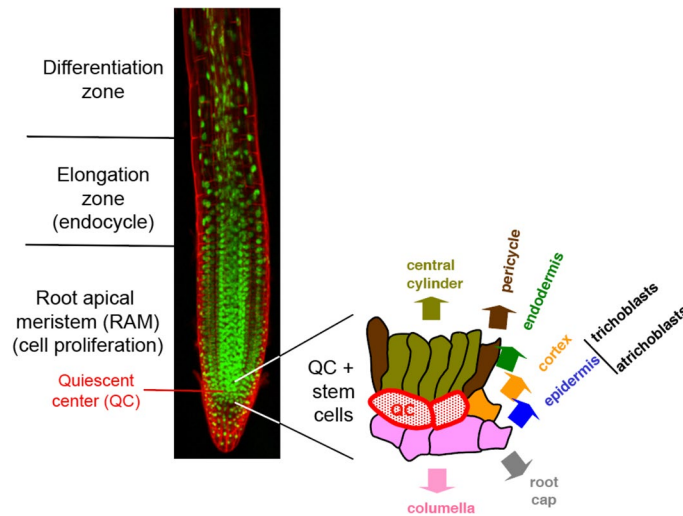
Peer review information *Nature Plants* thanks Ari Pekka Mähönen and the other, anonymous, reviewer(s) for their contribution to the peer review of this work.

Reprints and permissions information is available at www.nature.com/reprints.

Publisher's note Springer Nature remains neutral with regard to jurisdictional claims in published maps and institutional affiliations.

Open Access This article is licensed under a Creative Commons Attribution-NonCommercial-NoDerivatives 4.0 International License, which permits any non-commercial use, sharing, distribution and reproduction in any medium or format, as long as you give appropriate credit to the original author(s) and the source, provide a link to the Creative Commons licence, and indicate if you modified the licensed material. You do not have permission under this licence to share adapted material derived from this article or parts of it. The images or other third party material in this article are included in the article's Creative Commons licence, unless indicated otherwise in a credit line to the material. If material is not included in the article's Creative Commons licence and your intended use is not permitted by statutory regulation or exceeds the permitted use, you will need to obtain permission directly from the copyright holder. To view a copy of this licence, visit <http://creativecommons.org/licenses/by-nc-nd/4.0/>.

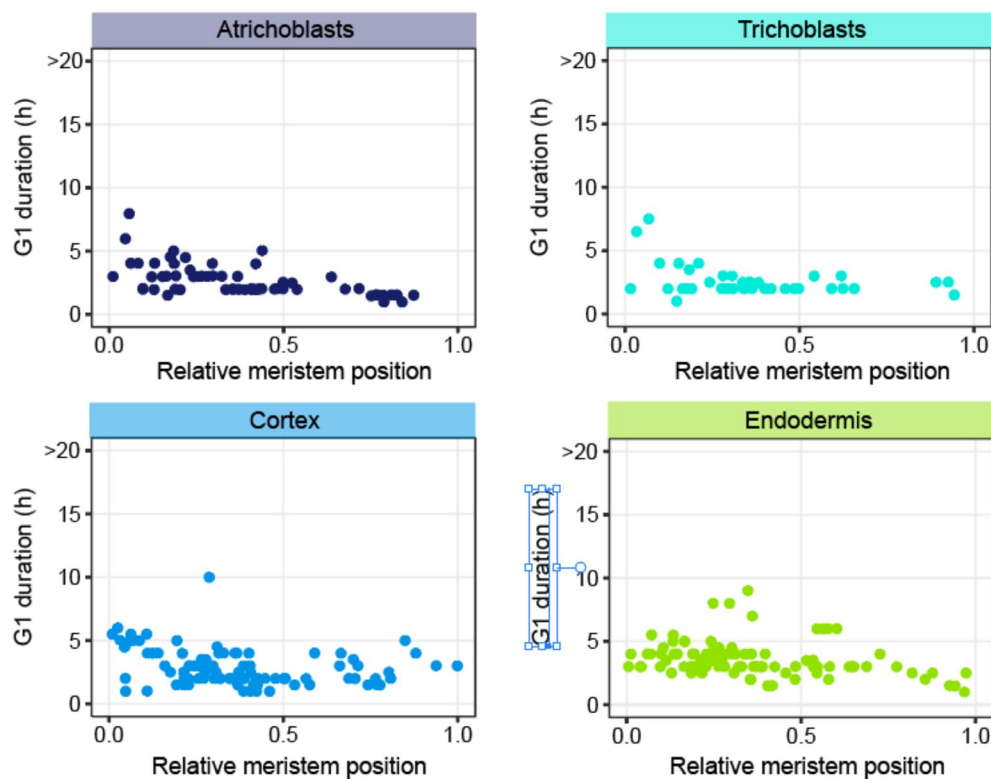
© The Author(s) 2025



Extended Data Fig. 1 | Anatomical organization of the *Arabidopsis* root apex.

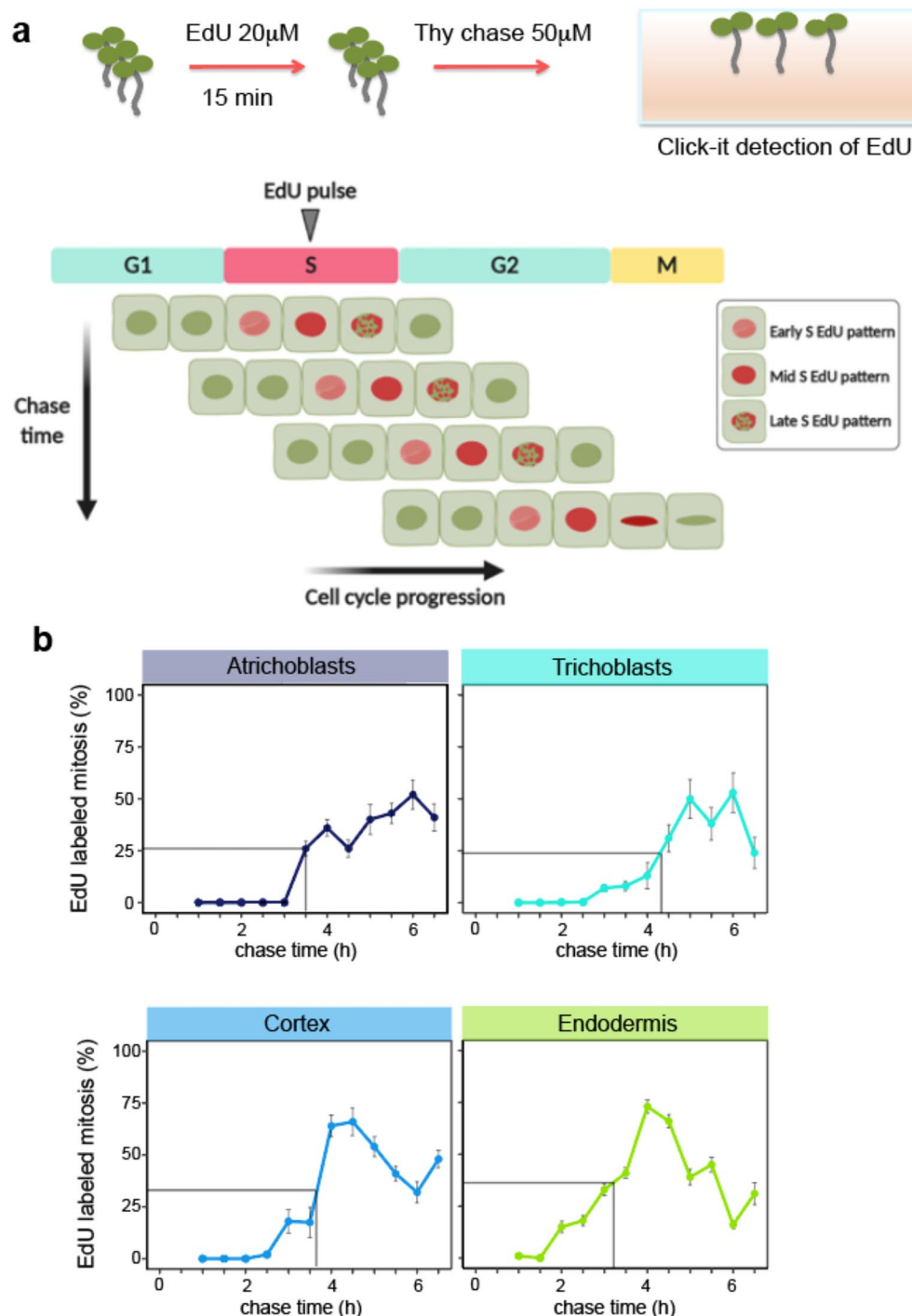
Nuclei are identified by the constitutive expression of a histone H3.3-GFP protein (green) and the cell walls were stained with propidium iodide. On the radial axis, concentric cell layers can be identified from the outermost epidermal layer to the cortex, endodermis, pericycle and vascular tissues. On the longitudinal axis, the root apical meristem (RAM), the focus of our study, occupies the more distal (or rootward) zone and contains all proliferating cells⁵². The RAM is followed by an elongation zone, where cells stop proliferation, enter the endocycle and

initiate elongation, and finally a differentiation zone where cells acquire their final differentiated state. Within the RAM, a group of rarely dividing cells, the quiescent center (QC) cells, is located distally and is surrounded by stem cells^{53,54} that give rise to all different root cell types (see inset). Asymmetric division of these stem cells renders the first derivatives that undergo several divisions within the transit amplifying compartment before arresting the cell cycle and initiating an elongation process, coinciding with the RAM boundary⁹, which is defined by a complex hormonal balance^{55,56}.



Extended Data Fig. 2 | Duration of G1 in various cell types in cells lacking the RBRI protein. Videos were recorded covering the RAM of plants expressing the PlaCCI markers in a mutant lacking RBRI (*rBRr* plants), as described in the

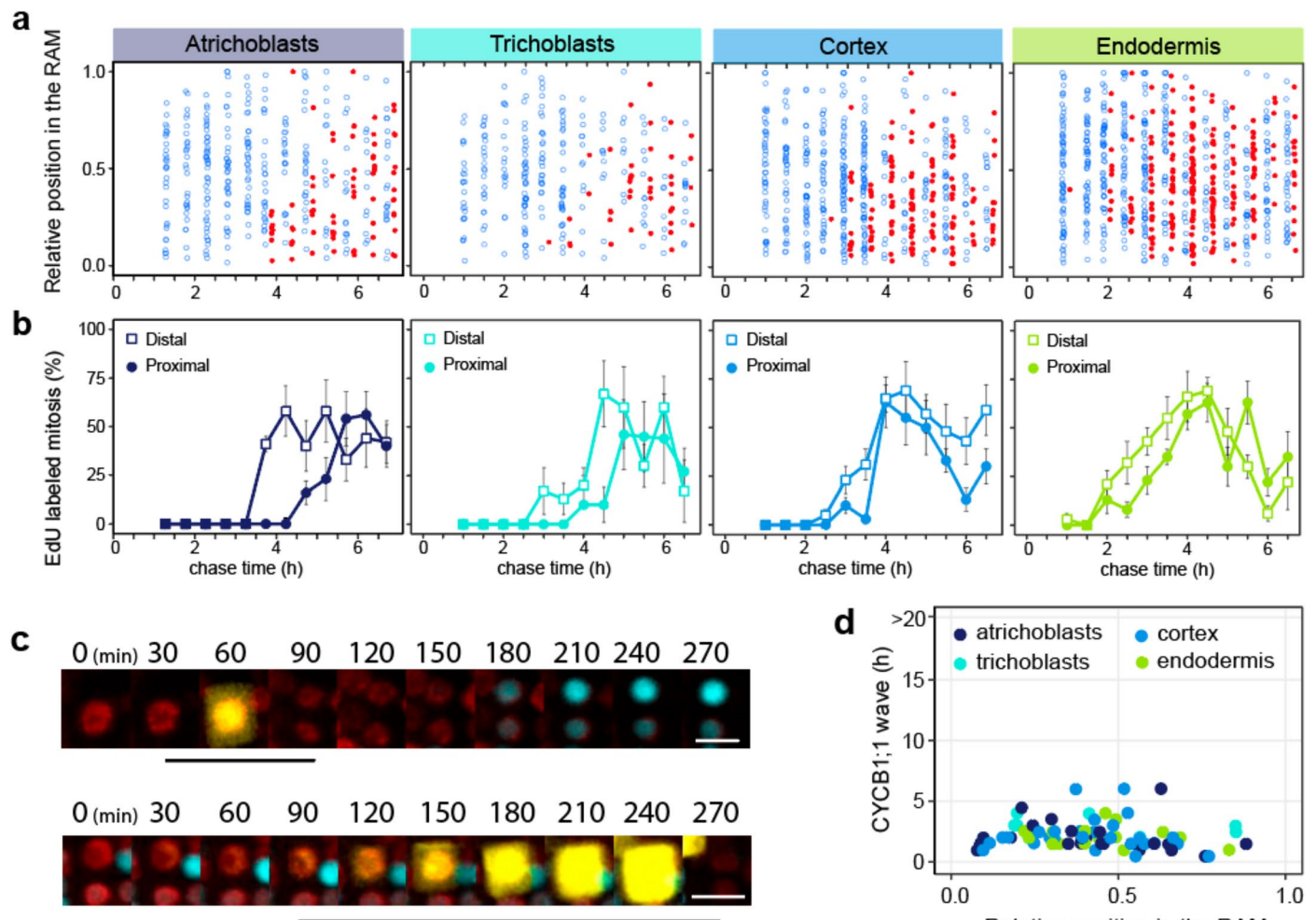
main text. Each dot represents the G1 length of individual cells. Cell numbers were 62, 44, 94 and 95 for atrichoblasts, trichoblasts, cortex and endodermis, respectively, taken from 9 roots.



Extended Data Fig. 3 | Measure of G2 phase duration in various cell types.

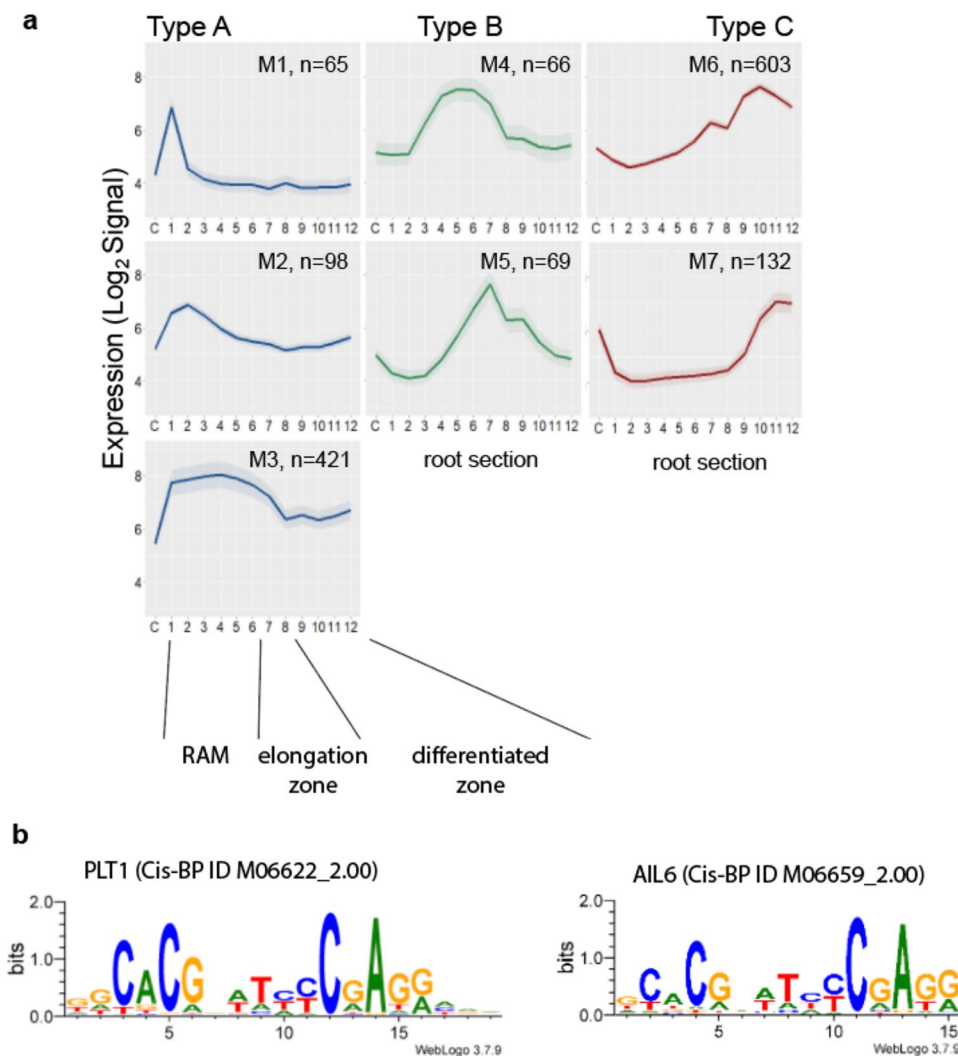
a, EdU pulse-chase strategy for direct measurement of the G2 phase duration. Seedlings were labeled with a short (15 min) pulse of the thymidine analogue EdU and then chased for different periods of time, in the absence of EdU and in the presence of an excess of thymidine to reduce further EdU incorporation, before Click-It detection of EdU labeled nuclei, as indicated in the upper part of the figure. The lower part of the figure contains a simplified scheme to illustrate cell cycle progression during the chase period. Cells in S-phase are all labeled with EdU during the pulse. Then, with time, cells progress across G2 and eventually enter mitosis. Quantification of mitotic cells labeled with EdU in the different chase times measures the G2 length. The average G2 phase duration

corresponds to the chase time where 50% of mitotic cells appear labeled, assuming a normal distribution of the EdU labeled cells. **b**, Average duration of G2 in various cell types. The fraction of EdU-labeled mitosis was quantified at different chase times after a pulse with EdU (15 min) by counting labeled (red) and unlabeled (blue) mitotic figures in individual roots ($n = 10$ per time point). The percentage of labeled mitoses was calculated for each root, and the mean \pm SD is shown. The average G2 duration was estimated as the time point at which 50% of the maximum number of EdU-labeled mitotic figures was reached in the pulse-chase curve (indicated by the thin lines in each case). Panel **a** created with [BioRender.com](https://www.biorender.com).



Extended Data Fig. 4 | Differences in G2 duration do not compensate for the long G1. a, G2 progression by measuring the appearance of mitotic cells labeled after an EdU pulse (15 min). Unlabeled (blue dots) and labeled (red dots) mitosis were scored at various chase times after the EdU pulse, according to their position along the RAM (0.0 = QC, 1.0 = RAM boundary, as described in Fig. 1c). Quantifications were carried out separately for various cell types, as indicated. **b**, Quantification of EdU-labeled mitosis at various chase times in two regions of the RAM: distal (empty squares) corresponds to the region located between the position 0.0 (QC) up to 0.4 of the RAM; proximal (filled circles) includes the rest of the RAM (from 0.4 to its boundary at 1.0). Data are mean values \pm s.d. The experiment was carried out in duplicate, processing 5 roots per biological replicate for each chase time. Total number of cells analyzed for each cell type

was: atrichoblasts (n = 312 EdU⁻, n = 75 EdU⁺), trichoblasts (n = 237 EdU⁻, n = 42 EdU⁺), cortex (n = 401 EdU⁻, n = 139 EdU⁺), endodermis (n = 495 EdU⁻, n = 237 EdU⁺). **c**, Live-imaging of cells showing the dynamics of CYCB1;1 loading in late G2 and its degradation at the metaphase/anaphase transition. Two examples of cells with a relatively short (upper panel; atrichoblast located at relative position 0.41 of the RAM) and long (lower panel; trichoblast at position 0.37) G2+prophase+metaphase period (black bars under each panel) are shown. Scale bar = 10 μ m. **d**, Duration of the CYCB1;1 wave (time between first detectable signal and complete degradation of CYCB1;1 at the metaphase/anaphase transition) along the root meristem in four root cell types, as indicated. Total n = 75 cells, 4 roots.

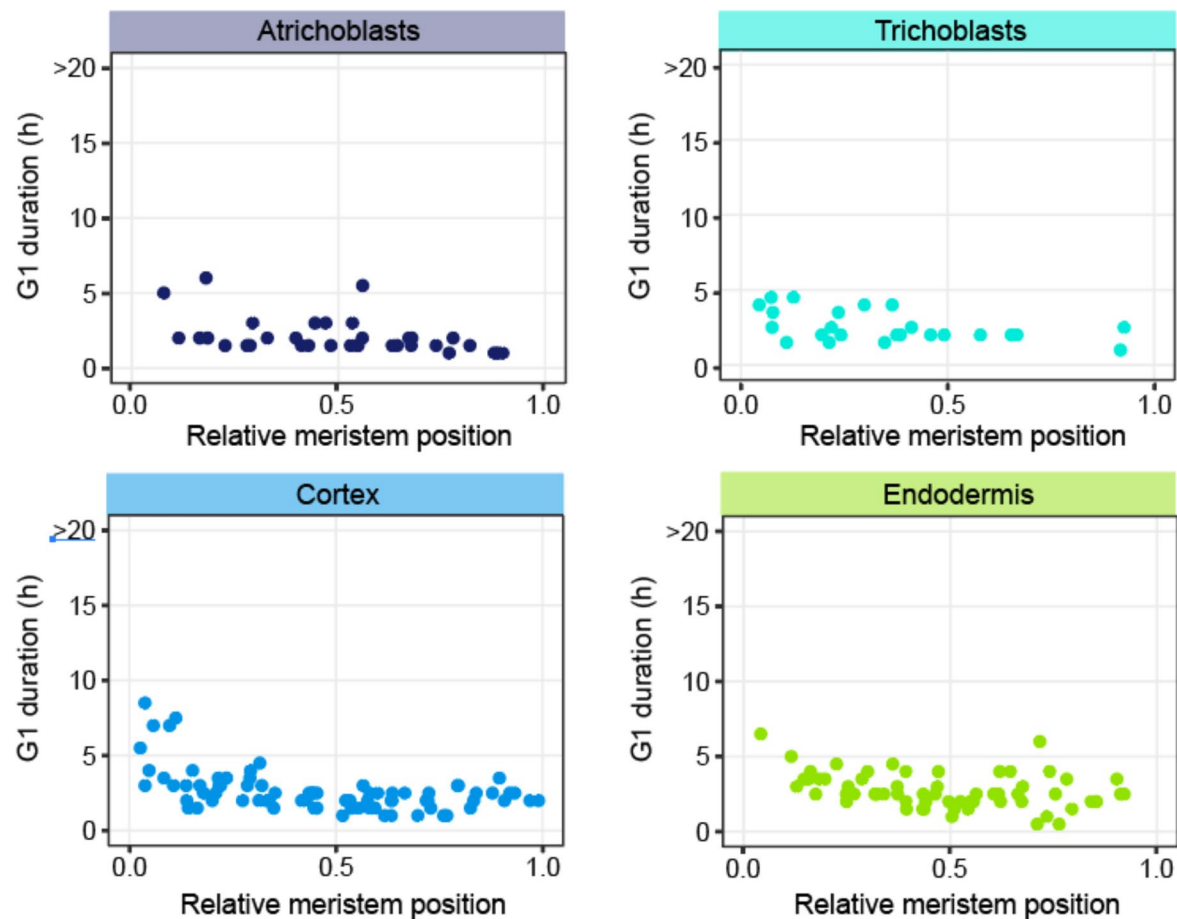


Extended Data Fig. 5 | Analysis of gene regulatory network along the root.

a, A WGCNA clustering in relation to gene expression along the root. Root sections were taken from Brady et al.¹⁷ where C corresponds to the columella and the RAM boundary to section 6. Plots represent mean gene expression (and confidence interval in shade) of the genes included in each of the modules or clusters. The number of genes is indicated as 'n'. Gene modules are classified in relation to their maximal expression in distal (type A), middle (type B) and proximal (type C)

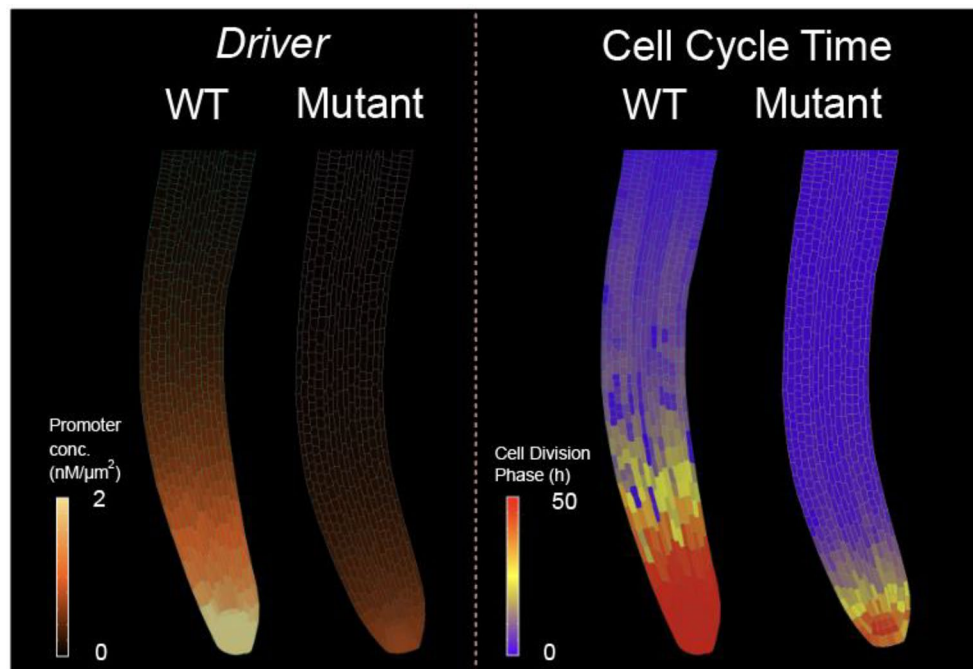
root sections (Section C = columella; sections 1-6 = RAM; sections 7-8 = transition (endoreplication) zone; sections 9-12 = elongation-differentiation zone).

b, AP2-ANT binding sites enriched in M1 promoters corresponded to PLT1 (Cis-BP ID M06622_2.00) and AIL6 (Cis-BP ID M06659_2.00) with consensus sequences kgCACGrwtyyCgAGmrr and gCaCGrwTyyCgAkr, respectively. Nucleotide codes are as follows: K, G or T; R, A or G; W, A or T; Y, C or T; M, A or C.

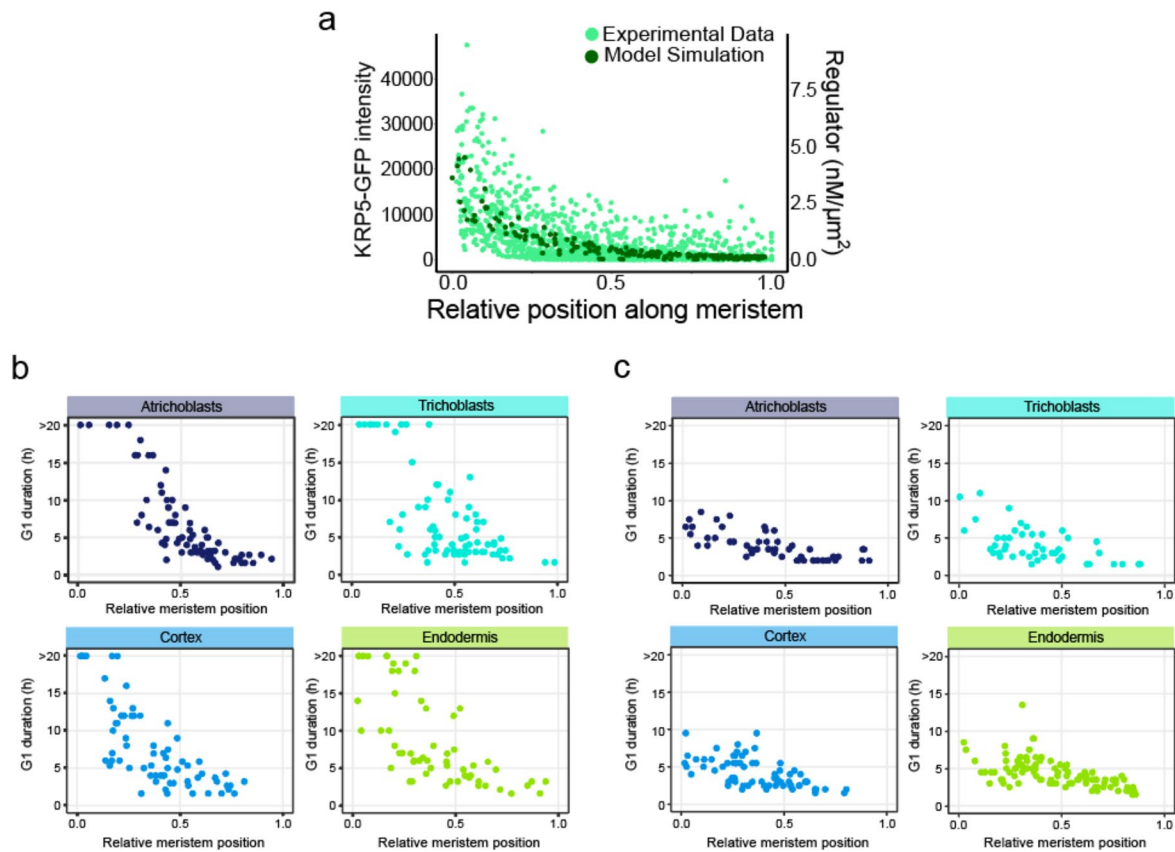


Extended Data Fig. 6 | Duration of G1 in various cell types in cells of *plt1-4, plt2-2* double mutant. Videos were recorded covering the RAM of plants expressing the PlaCC1 markers in a *plt1-4, plt2-2* double mutant, as described in

the main text. Each dot represents the G1 length of individual cells. Cell numbers were 36, 26, 81 and 64 for atrichoblasts, trichoblasts, cortex and endodermis, respectively from 2 roots.

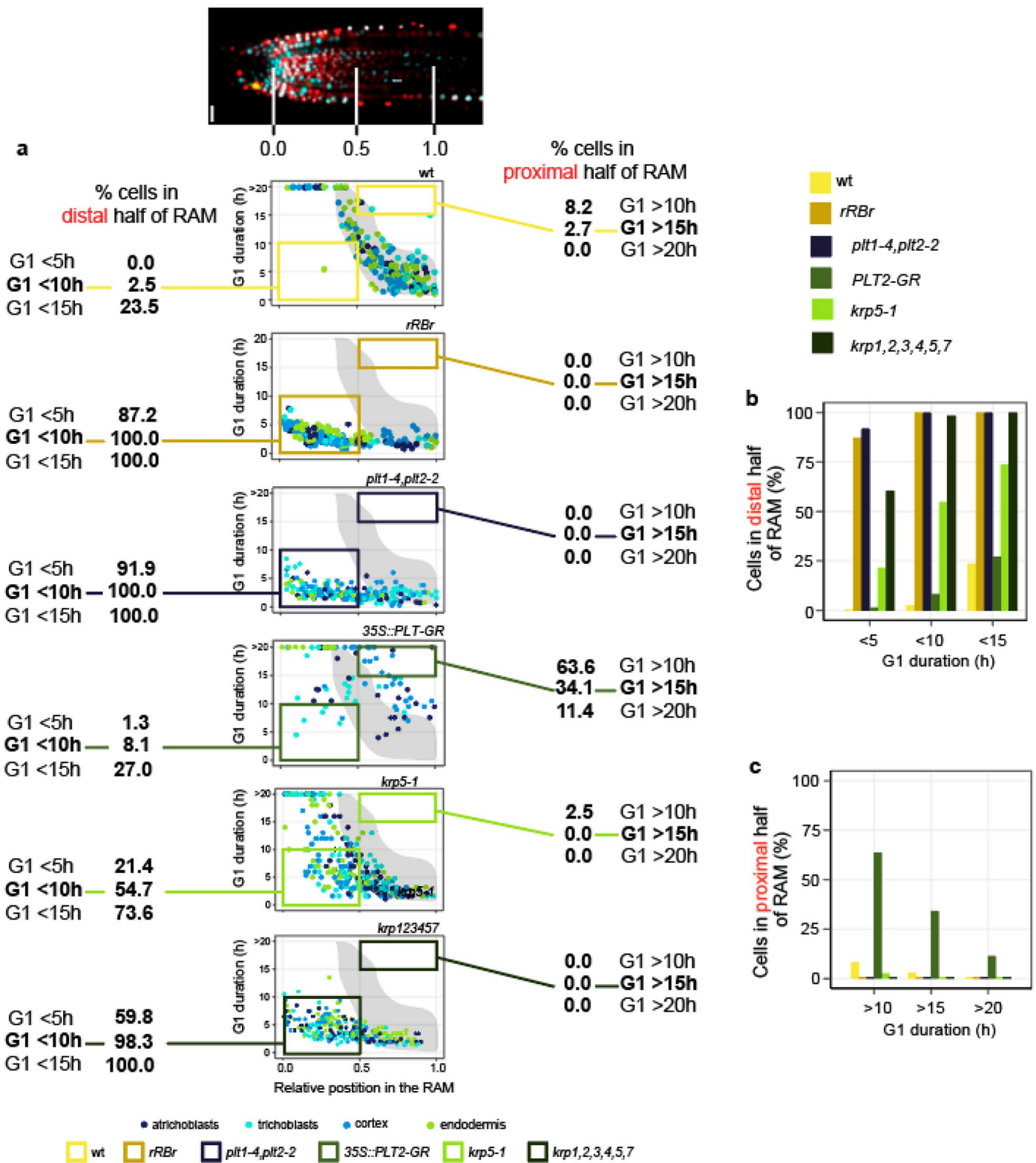


Extended Data Fig. 7 | Simulations of PLT mutant predict shortening of G1 duration with reduction of IFFL driver. Left panel: model simulation showing *driver* activity in the wild type and *plti-4,plt2-2* mutant. Right panel: model simulation showing cell cycle time (a proxy of G1 duration in our model) along the root as a result of *driver* accumulation in the wild type and the mutant.



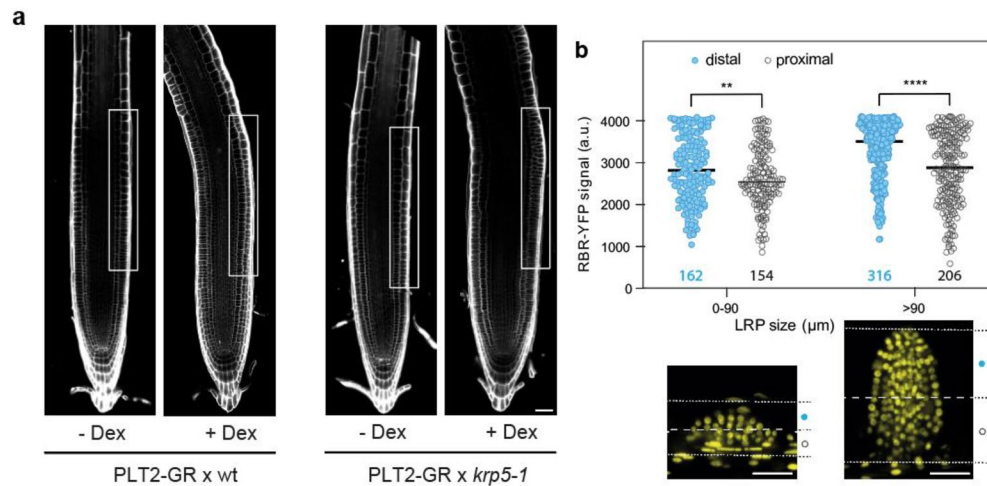
Extended Data Fig. 8 | Modeling KRP5 expression and G1 duration in *krp* mutants. **a**, Comparison between model simulation and experimental data of the KRP5-GFP signal. Experimental KRP5-GFP data (light green dots) with model simulation data (dark green dots). Each dot represents the value of individual cells. **b**, Duration of G1 in various cell types in cells of *krp5-1* mutant. Videos were recorded covering the RAM of plants expressing the PlaCCI markers in the *krp5-1* mutant, as described in the main text. Each dot represents the G1

length of individual cells. Cell numbers were 78, 73, 68 and 59 for atrichoblasts, trichoblasts, cortex and endodermis, respectively (6 roots). **c**, Duration of G1 in various cell types in cells of the sextuple *krp1,2,3,4,5,7* mutant. Videos were recorded covering the RAM of plants expressing the PlaCCI markers in the *krp1,2,3,4,5,7* mutant, as described in the main text. Each dot represents the G1 length of individual cells. Cell numbers were 51, 45, 69 and 99 for atrichoblasts, trichoblasts, cortex and endodermis, respectively (2 roots).



Extended Data Fig. 9 | Summary of G1 duration in the genetic backgrounds studied. a, Percentage of cells with G1 duration of the indicated lengths in the distal (between relative position 0.0 and 0.5) and proximal (between relative position 0.5 and 1.0) halves of the RAM in each genotype analyzed in this study.

b, Summary of percentage of cells with different G1 durations located in the distal half of the RAM in each genotype analyzed in this study. **c,** Summary of percentage of cells with different G1 durations located in the proximal half of the RAM in each genotype analyzed in this study.



Extended Data Fig. 10 | Root phenotype after PLT2 expression and expression pattern of RBR-YFP in lateral roots. a, Effect of constitutive PLT2 expression on cell division. Whole root meristems of 6 day old plants expressing PLT2-GR in wild type (wt) or *krp5-1* mutant background in the presence or absence of Dexamethasone (Dex) during 30 h. Details of the epidermal layer of each case (white rectangles) are shown in Fig. 3f. Scale bar = 20 μm. **b**, Quantification of RBR in lateral root primordia (LRP). LRPs of plants expressing RBR-YFP were classified depending on their size in early (0-90 μm) and late (≥ 90 μm) stage of development. For quantification, LRPs of seedlings expressing RBR-YFP were

divided into two halves: the distal half (solid blue circles), towards the apex of the LRPs and the proximal half (empty circles), towards the base of LRPs. Data points correspond to RBR-YFP signal intensity of individual cells and the median is represented. The number of cells recorded are indicated for each LRP size class below each data distribution inside the graph. The number of LRPs scored for each size class was: 0-90 (n = 8), >90 (n = 5) from 3 roots. Statistical significance was determined using Mann-Whitney Rank Sum tests (two sided): **, p < 0.01; ****, p < 0.0001. Representative images of the lateral root primordia analyzed at different development stages are shown below the graph. Scale bar = 40 μm.

Reporting Summary

Nature Portfolio wishes to improve the reproducibility of the work that we publish. This form provides structure for consistency and transparency in reporting. For further information on Nature Portfolio policies, see our [Editorial Policies](#) and the [Editorial Policy Checklist](#).

Statistics

For all statistical analyses, confirm that the following items are present in the figure legend, table legend, main text, or Methods section.

n/a Confirmed

- ☐ ☒ The exact sample size (n) for each experimental group/condition, given as a discrete number and unit of measurement
- ☐ ☒ A statement on whether measurements were taken from distinct samples or whether the same sample was measured repeatedly
- ☐ ☒ The statistical test(s) used AND whether they are one- or two-sided
Only common tests should be described solely by name; describe more complex techniques in the Methods section.
- ☒ ☐ A description of all covariates tested
- ☒ ☐ A description of any assumptions or corrections, such as tests of normality and adjustment for multiple comparisons
- ☐ ☒ A full description of the statistical parameters including central tendency (e.g. means) or other basic estimates (e.g. regression coefficient) AND variation (e.g. standard deviation) or associated estimates of uncertainty (e.g. confidence intervals)
- ☒ ☐ For null hypothesis testing, the test statistic (e.g. F , t , r) with confidence intervals, effect sizes, degrees of freedom and P value noted
Give P values as exact values whenever suitable.
- ☒ ☐ For Bayesian analysis, information on the choice of priors and Markov chain Monte Carlo settings
- ☒ ☐ For hierarchical and complex designs, identification of the appropriate level for tests and full reporting of outcomes
- ☒ ☐ Estimates of effect sizes (e.g. Cohen's d , Pearson's r), indicating how they were calculated

Our web collection on [statistics for biologists](#) contains articles on many of the points above.

Software and code

Policy information about [availability of computer code](#)

Data collection

NIS Elements v5.30.02
ZenBlue v3.3.89.0000
BioRad CFX Maestro 2.2, version 5.2-008-0222

Data analysis

Fiji v1.53f51
Data in Fig. 2 were processed using WGCNA 1.69; ggplot2 3.3.3; limma 3.44.3; RStudio 1.3.959
Microsoft Excel 365 v2210
Graphs were generated using Ggplot2 package v3.4.0 running on R v3.6.3
Model simulation were performed using MorphoDynamX: <https://morphographx.org/morphodynamx/>, an improved version of MorphogGraphX (Barbier de Reuille et al, 2015 in the manuscript).
The computer model code implementation can be found here: <https://github.com/PDLABCBGP/ROOTMODEL-PBD>.

For manuscripts utilizing custom algorithms or software that are central to the research but not yet described in published literature, software must be made available to editors and reviewers. We strongly encourage code deposition in a community repository (e.g. GitHub). See the Nature Portfolio [guidelines for submitting code & software](#) for further information.

Data

Policy information about [availability of data](#)

All manuscripts must include a [data availability statement](#). This statement should provide the following information, where applicable:

- Accession codes, unique identifiers, or web links for publicly available datasets
- A description of any restrictions on data availability
- For clinical datasets or third party data, please ensure that the statement adheres to our [policy](#)

Previously published RNA-seq data reanalyzed here are detailed in the text and Fig. 2

Videos and images have been submitted. These together with any supporting information of our findings are available from the corresponding authors, on reasonable requests.

Human research participants

Policy information about [studies involving human research participants and Sex and Gender in Research](#).

Reporting on sex and gender	n/a
Population characteristics	n/a
Recruitment	n/a
Ethics oversight	n/a

Note that full information on the approval of the study protocol must also be provided in the manuscript.

Field-specific reporting

Please select the one below that is the best fit for your research. If you are not sure, read the appropriate sections before making your selection.

☒ Life sciences ☐ Behavioural & social sciences ☐ Ecological, evolutionary & environmental sciences

For a reference copy of the document with all sections, see [nature.com/documents/nr-reporting-summary-flat.pdf](https://www.nature.com/documents/nr-reporting-summary-flat.pdf)

Life sciences study design

All studies must disclose on these points even when the disclosure is negative.

Sample size	Quantifications performed on videos and confocal images were obtained using multiple plants, as indicated in legends and/or text. For each root cell type analyzed, the sample size is specified in the legends. Sample size was not estimated by statistical methods, but it was based on previous experience and on similar studies in this field.
Data exclusions	All raw data obtained throughout this study have been included in the analysis.
Replication	The number of biological replicates and/or the number of roots used are indicated in the figure legends. All replication attempts were successful.
Randomization	n/a
Blinding	n/a

Reporting for specific materials, systems and methods

We require information from authors about some types of materials, experimental systems and methods used in many studies. Here, indicate whether each material, system or method listed is relevant to your study. If you are not sure if a list item applies to your research, read the appropriate section before selecting a response.

Materials & experimental systems

n/a	Involved in the study
<input checked="" type="checkbox"/>	<input type="checkbox"/> Antibodies
<input checked="" type="checkbox"/>	<input type="checkbox"/> Eukaryotic cell lines
<input checked="" type="checkbox"/>	<input type="checkbox"/> Palaeontology and archaeology
<input checked="" type="checkbox"/>	<input type="checkbox"/> Animals and other organisms
<input checked="" type="checkbox"/>	<input type="checkbox"/> Clinical data
<input checked="" type="checkbox"/>	<input type="checkbox"/> Dual use research of concern

Methods

n/a	Involved in the study
<input checked="" type="checkbox"/>	<input type="checkbox"/> ChIP-seq
<input checked="" type="checkbox"/>	<input type="checkbox"/> Flow cytometry
<input checked="" type="checkbox"/>	<input type="checkbox"/> MRI-based neuroimaging